

1 Hotspot *ESR1* mutations are multimodal and contextual 2 modulators of breast cancer metastasis

3 Zheqi Li (1, 2), Yang Wu (2, 3), Megan E. Yates (2, 4, 5), Nilgun Tasdemir (1, 2), Amir
4 Bahreini (2, 6), Jian Chen (2), Kevin M. Levine (2, 7), Nolan M. Priedigkeit (1, 2),
5 Azadeh Nasrazadani (2), Simak Ali (8), Laki Buluwela (8), Spencer Arnesen (9, 10),
6 Jason Gertz (9, 10), Jennifer K. Richer (11), Benjamin Troness (12), Dorraya El-Ashry
7 (12), Qiang Zhang (13), Lorenzo Gerratana (13, 14), Youbin Zhang (13), Massimo
8 Cristofanilli (13), Maritza A. Montanez (15), Prithu Sundd (15), Callen T. Wallace (16),
9 Simon C. Watkins (16), Caterina Fumagalli (17), Elena Guerini-Rocco (17, 18), Li Zhu
10 (19), George C. Tseng (19), Nikhil Wagle (20), Jason S. Carroll (21), Paul Jank (22),
11 Carsten Denkert (22), Maria M Karsten (23) , Jens-Uwe Blohmer (23), Ben H. Park (24),
12 Peter C. Lucas (7), Jennifer M. Atkinson (1,2), Adrian V. Lee (1, 2, 4, 6), Steffi
13 Oesterreich* (1, 2, 4, 6, 7)

- 14 1. Department of Pharmacology and Chemical Biology, University of Pittsburgh,
15 Pittsburgh PA, USA
- 16 2. Women's Cancer Research Center, Magee Women's Research Institute, UPMC
17 Hillman Cancer Center, Pittsburgh PA, USA
- 18 3. School of Medicine, Tsinghua University, Beijing, China
- 19 4. Integrative Systems Biology Program, University of Pittsburgh, Pittsburgh, PA,
20 USA.
- 21 5. Medical Scientist Training Program, University of Pittsburgh School of Medicine,
22 Pittsburgh, PA, USA.
- 23 6. Department of Human Genetics, University of Pittsburgh, Pittsburgh PA, USA
- 24 7. Department of Pathology, University of Pittsburgh, Pittsburgh PA, USA
- 25 8. Department of Surgery and Cancer, Imperial College London, London, UK
- 26 9. Department of Oncological Sciences, University of Utah, Salt Lake City, UT, USA
- 27 10. Huntsman Cancer Institute, University of Utah, Salt Lake City, UT, USA
- 28 11. Department of Pathology, University of Colorado Anschutz Medical Campus,
29 Aurora, CO, USA
- 30 12. University of Minnesota Masonic Cancer Center, Minneapolis, MN, USA

- 31 13. Robert H. Lurie Cancer Center of Northwestern University, Feinberg School of
32 Medicine, Chicago, IL, US
- 33 14. Department of Medicine (DAME) University of Udine, Udine, Italy
- 34 15. Pittsburgh Heart, Lung and Blood Vascular Medicine Institute, University of
35 Pittsburgh School of Medicine, Pittsburgh PA, USA
- 36 16. Center for Biological Imaging, University of Pittsburgh, Pittsburgh PA, USA
- 37 17. Division of Pathology and Laboratory Medicine, IEO, European Institute of
38 Oncology, IRCCS, Milan, Italy
- 39 18. Department of Oncology and Hemato-Oncology, University of Milan, Milan, Italy
- 40 19. Department of Biostatistics, University of Pittsburgh, Pittsburgh PA, USA
- 41 20. Department of Medical Oncology and Center for Cancer Precision Medicine, Dana-
42 Farber Cancer Institute, Harvard Medical School, Brigham and Women's Hospital,
43 Boston, MA, USA
- 44 21. Cancer Research UK, Cambridge Institute, University of Cambridge, Cambridge,
45 UK
- 46 22. Institut of Pathology, Philipps-University Marburg, UKGM - Universitätsklinikum
47 Marburg, Marburg, Germany
- 48 23. Department of Gynecology with Breast Center, Charité – Universitätsmedizin
49 Berlin, Corporate member of Freie Universität Berlin, Humboldt-Universität zu
50 Berlin and Berlin Institute of Health, Berlin, Germany
- 51 24. Vanderbilt University Inghram Cancer Center, Nashville, TN, USA

52

53 *Corresponding Author:

54 Steffi Oesterreich, PhD

55 Mailing address: Magee Women's Research Institute, B411

56 204 Craft Avenue, Pittsburgh, PA, 15213

57 Email: oesterreichs@upmc.edu

58

59 **Running Title**

60 *ESR1* mutations facilitate breast cancer metastasis

61

62 **Key Words**

63 *ESR1* mutations, Metastasis, Cell Adhesion, Migration, Breast cancer

64

65 **Financial Support**

66 This work was supported by the Breast Cancer Research Foundation (AVL, BHP and
67 SO); Susan G. Komen Scholar awards (SAC110021 to AVL, SAC170078 to BHP,
68 SAC160073 to SO); the Metastatic Breast Cancer Network Foundation [SO]; the
69 National Cancer Institute (R01CA221303 to SO, F30CA203154 to KML, F30CA250167
70 to MEY); Department of Defense Breast Cancer Research Program (W81XWH1910434
71 to JG and W81XWH1910499 to SO), and the Fashion Footwear Association of New
72 York, Magee-Women's Research Institute and Foundation, The Canney Foundation,
73 The M&E Foundation, Nicole Meloche Foundation, Penguins Alumni Foundation, the
74 Pennsylvania Breast Cancer Coalition and the Shear Family Foundation. SO and AVL
75 are Hillman Fellows. ZL is supported by John S. Lazo Cancer Pharmacology
76 Fellowship. NT was supported by a Department of Defense Breakthrough Fellowship
77 Award [BC160764] and an NIH Pathway to Independence Award [K99CA237736]. This
78 project used the UPMC Hillman Cancer Center Tissue and Research Pathology
79 Services supported in part by NIH grant award P30CA047904.

80

81 **Conflict of Interest Disclosure Statement**

82 SO and AVL receive research support from AstraZeneca PLC. AVL is employee and
83 consultant with UPMC Enterprises, and member of the Scientific Advisory Board,
84 Stockholder and receives compensation from Ocean Genomics. Tsinghua University
85 paid the stipend of University of Pittsburgh-affiliated foreign scholar Yang Wu from
86 Tsinghua University. MC serves for Pfizer (research support, honoraria), Lilly (advisor,
87 honoraria); Foundation Medicine (honoraria); Sermonix (advisor), G1Therapeutics
88 (advisor) and CytoDyn (advisor). LG receives travel expenses from Menarini SB. BHP
89 has ownership interest and is a paid member of the scientific advisory board of Loxo
90 Oncology and is a paid consultant for Foundation Medicine, Inc, Jackson Labs, Roche,
91 Eli Lilly, Casdin Capital, Astra Zeneca and H3 Biomedicine, and has research funding
92 from Abbvie, Pfizer and Foundation Medicine, Inc. Under separate licensing

93 agreements between Horizon Discovery, LTD and The Johns Hopkins University, BHP
94 is entitled to a share of royalties received by the University on sales of products. The
95 terms of this arrangement are being managed by The Johns Hopkins University in
96 accordance with its conflict-of-interest policies. CD reports grants from European
97 Commission H2020, grants from German Cancer Aid Translational Oncology, during the
98 conduct of the study; personal fees from Novartis, personal fees from Roche, personal
99 fees from MSD Oncology, personal fees from Daiichi Sankyo, personal fees from
100 AstraZeneca, from Molecular Health, grants from Myriad, personal fees from Merck,
101 other from Sividon diagnostics, outside the submitted work. In addition, CD has a
102 patent VMScope digital pathology software with royalties paid, a patent
103 WO2020109570A1 - cancer immunotherapy pending, and a patent WO2015114146A1
104 and WO2010076322A1- therapy response issued. PJ reports other support from
105 Myriad Genetics, Inc. which is outside the submitted work.

106 **Abstract**

107 Constitutively active estrogen receptor- α (ER/*ESR1*) mutations have been identified in
108 approximately one third of ER+ metastatic breast cancers. Although these mutations are known
109 mediators of endocrine resistance, their potential role in promoting metastatic disease has not
110 yet been mechanistically addressed. In this study, we show the presence of *ESR1* mutations
111 exclusively in distant but not local recurrences in five independent breast cancer cohorts. In
112 concordance with transcriptomic profiling of *ESR1* mutant tumors, genome-edited *ESR1* Y537S
113 and D538G mutant cell models exhibited a reprogrammed cell adhesive gene network via
114 alterations in desmosome/gap junction genes and the TIMP3/MMP axis, which functionally
115 conferred enhanced cell-cell contacts while decreasing cell-extracellular matrix (ECM) adhesion.
116 In vivo studies showed *ESR1* mutant cells were associated with larger multi-cellular circulating
117 tumor cell (CTC) clusters with increased compactness compared to *ESR1* WT CTCs. These
118 preclinical findings translated to clinical observations, where CTC clusters were enriched in
119 patients with *ESR1*-mutated metastatic breast cancer. Conversely, context-dependent migratory
120 phenotypes revealed co-targeting of Wnt and ER as a vulnerability in a D538G cell model.
121 Mechanistically, mutant *ESR1* exhibited non-canonical regulation of several metastatic
122 pathways, including secondary transcriptional regulation and de novo FOXA1-driven chromatin
123 remodeling. Collectively, these data provide evidence for *ESR1* mutation-modulated metastasis
124 and suggest future therapeutic strategies for targeting *ESR1* mutant breast cancer.

125

126 **Statement of Significance**

127 Context and allele-dependent transcriptome and cistrome reprogramming in mutant *ESR1* cell
128 models elicit diverse metastatic phenotypes related to cell adhesion and migration, which can
129 be pharmacologically targeted in metastatic breast cancer.

130

131 **Introduction**

132 More than 70% of breast cancers express estrogen receptor- α (ER/*ESR1*). Antiestrogen
133 therapies, including depletion of estradiol (E2) by aromatase inhibitors (AIs) or
134 antagonizing ER activity by Selective Estrogen Receptor Modulators/Degraders
135 (SERMs/SERDs), are conventional treatments for ER+ breast cancer. Development of
136 resistance to these endocrine therapies, however, remains a clinical and socioeconomic
137 challenge (1,2).

138 30-40% of endocrine-resistant metastatic breast cancer (MBC) is enriched in *ESR1*
139 somatic base pair missense mutations (3-5), that can be detected in the blood of
140 patients with advanced disease (6,7). Clinically, ligand binding domain (LBD) *ESR1*
141 mutations correlate with poor outcomes in patients with advanced disease (6,8,9).
142 Recent work from our group and others has uncovered a crucial role for these *ESR1*
143 hotspot mutations in driving constitutive ER activity and decreased sensitivity towards
144 ER antagonists (10-12). Moreover, structural investigation of the two most frequent
145 mutations, variants Y537S and D538G, has demonstrated that *ESR1* mutations stabilize
146 helix 12 (H12) in an agonist conformation, thereby providing a mechanistic explanation
147 for constitutive ER activity (13).

148 The identification of *ESR1* mutations in endocrine resistant MBC suggests that mutant
149 ER may not only mediate endocrine resistance but also have an unappreciated role in
150 enabling metastasis. Indeed, recent *in vivo* studies showed that mutant ER can promote
151 metastasis (14,15), and *in vitro* studies showed a gain of cell motility (15,16) and growth
152 in 3D culture (17). Although epithelial-mesenchymal transition (EMT) has been
153 described as one potential explanation for the Y537S mutant (18), overall mechanisms
154 remain largely unclear. In order to identify personalized therapeutic vulnerabilities in
155 patients harboring *ESR1* hotspot mutations, there is an urgent need to decipher the
156 mechanistic underpinnings and precise roles of mutant ER in the metastatic progression
157 using comprehensive approaches and model systems.

158 Previous transcriptomic profiling performed by us and others has revealed a context-
159 dependence of *ESR1* mutation effects, as well as significant differences between the
160 two most frequent hotspot mutations, Y537S and D538G (11,12,14,15,19). Differentially

161 expressed genes vary widely following expression of the mutations in their respective
162 cell line model, however, both Y537S and D538G maintain distinction from the E2-
163 dependent wild-type (WT) ER transcriptome. Similarly, comparison of the WT and
164 mutant ER cistromes has also revealed context-dependent and allele-specific effects on
165 ER recruitment (11,14). Furthermore, we recently showed that *ESR1*-mutant
166 transcriptomic reprogramming is associated with epigenetic remodeling (19). While
167 these findings imply that in the setting of high molecular diversity in tumors and patients,
168 somatic *ESR1* mutations have the potential to trigger different metastatic phenotypes,
169 this phenomenon has yet to be investigated.

170 In this study, we explore metastatic gain-of-function phenotypes in genome-edited
171 *ESR1* mutant models under the guidance of transcriptomic changes detected in clinical
172 samples. We identify mechanisms underlying context and allele-specific metastatic
173 phenotypes, and subsequently confirm alterations in a number of potential therapeutic
174 targets in metastatic tumors. We believe that our systematic bedside-to-bench approach
175 will ultimately lead to improved metastasis-free outcomes and prognosis for patients
176 with ER+ tumors.

177

178 **Materials and methods**

179 Additional details and references are provided in the Supplementary Materials and
180 Methods section.

181 **Human tissue studies from the Womens Cancer Research Center (WCRC) and**
182 **Charite cohorts**

183 All patients enrolled were approved within IRB protocols (PRO15050502) from the
184 University of Pittsburgh and Charite Universitaetsmedizin Berlin. Informed consent was
185 obtained from all participating patients. Biopsies were obtained and divided into distant
186 metastatic or local recurrent tumors. Genomic DNA was isolated from formalin fixed
187 paraffin embedded (FFPE) samples and *ESR1* mutation status was detected with
188 droplet digital PCR (ddPCR) targeting Y537S/C/N and D538G mutations in pre-
189 amplified *ESR1* LBD products as previously reported (7).

191 **CTCs analysis from the NU16B06 Cohort**

192 A retrospective cohort comprising 151 Metastatic Breast Cancer (BC) patients
193 characterized for CTCs, and ctDNA at the Robert H. Lurie Comprehensive Cancer
194 Center of Northwestern University (Chicago, IL) between 2015 and 2019 was analyzed.
195 Patients' enrollment was performed under the Investigator Initiated Trial (IIT) NU16B06
196 independently from treatment line. The overall baseline staging was performed
197 according to the investigators' choice, CTCs and ctDNA collection was performed prior
198 to treatment start. CTC enumeration was performed though the CellSearch™
199 immunomagnetic System (Menarini Silicon Biosystems). Mutations in *ESR1* (hotspots
200 D538 and Y537) and PIK3CA (hotspots E453 and H1047) were detected by either
201 ddPCR assay using the QX200 ddPCR System (Bio-Rad) or through the
202 Guardant360™ high sensitivity next-generation sequencing platform (Guardant Health,
203 CA). More details for CTC enumeration, mutation detection and statistical analysis can
204 be found in Supplementary Materials and Methods.

206 **Cell culture**

207 Genome-edited MCF7 (RRID: CVCL_0031) and T47D (RRID: CVCL_0553) *ESR1*
208 mutant cell models from different sources were maintained as previously described

209 (12,19,20). Hormone deprivation was performed for all experiments, unless otherwise
210 stated.

211

212 **Reagents**

213 17 β -estradiol (E2, #E8875) was obtained from Sigma, and Fulvestrant (#1047),
214 carbenoxolone disodium (#3096) and EDTA (#2811) were purchased from Tocris.
215 LGK974 (#14072) and T-5224 (#22904) were purchased from Cayman. Marimastat
216 (S7156) was obtained from SelleckChem. Recombinant human Wnt3A (5036-WN-010)
217 was purchased from R&D Systems. For knockdown experiments, siRNA against
218 *FOXA1* (#M-010319), *DSC1* (#L-011995), *DSC2* (#L-011996), *GJA1* (#L-011042) and
219 *GJB2* (#L-019285) were obtained from Horizon Discovery. Desmosome and scramble
220 peptides were designed based on previous studies (21,22) and synthesized from
221 GeneScript. Peptide sequences are presented in Supplementary Table S10.

222

223 **Animal Studies**

224 **Long term metastatic evaluation:** 4-week old female *nu/nu* athymic mice were
225 ordered from The Jackson Laboratory (002019 NU/J, RRID: IMSR_JAX:002019)
226 according to University of Pittsburgh IACUC approved protocol #19095822. MCF7 and
227 T47D *ESR1* mutant cells were hormone deprived and resuspended in PBS with a final
228 concentration of 10⁷ cells/ml. 100 μ l of cell suspension was then injected via tail vein into
229 nude mice with 7 mice per group. Mice were under observation weekly. According to the
230 IACUC protocol, if greater than 50% of mice in any group show predefined signs of
231 euthanasia, the entire cohort needs to be euthanized. Cohorts were euthanized at 13
232 weeks for MCF7 cell-injected mice and 23 weeks for T47D cell-injected mice. Macro-
233 metastatic tumors and potential organs (lung, liver, UG tract) for metastatic spread were
234 harvested. Solid macro-metastatic tumors (non-lymph node) were counted for
235 comparison. All tissues were processed for FFPE preparation and hematoxylin and
236 eosin (H&E) staining by the Histology Core at Magee Women's Research Institute.
237 Macro-metastatic tumor FFPE sections were further evaluated by a trained pathologist.
238 Micro-metastatic lesions in the lung were further examined and quantified by
239 immunofluorescence staining as described in supplementary materials and methods.

240 **Short term CTC cluster assessment:** 4-week old female *nu/nu* athymic mice were
241 ordered from The Jackson Laboratory (002019 NU/J) according to University of
242 Pittsburgh IACUC approved protocol #19095822. MCF7 WT and mutant cells were
243 stably labelled with RFP-luciferase by infection with the pLEX-TRC210/L2N-TurboRFP-
244 c lentivirus plasmid. Labelled cells were hormone deprived and resuspended in PBS at
245 a final concentration of 10^7 cells/ml. 100 μ l of cell suspension was then injected into
246 nude mice with 6 mice per group via an intracardiac left ventricle injection. Post-injected
247 mice were immediately imaged using the IVIS200 *in vivo* imaging system (124262,
248 PerkinElmer) after D-luciferin intraperitoneal injection to confirm successful cell delivery
249 into the circulation system. All mice were euthanized after one hour of injection and their
250 whole blood were extracted via cardiac puncture and collected into CellSave
251 Preservative Tubes (#790005, CellSearch). Blood samples were mixed with 7ml of
252 RPMI media and shipped to University of Minnesota for CTC enrichment. CTCs were
253 extracted using an electric size-based microfilter system (FaCTChekr) and stained with
254 antibody against pan-cytokeratins (CK) and DAPI. Slides with stained CTCs were
255 manually scanned in a blind manner and all visible single CTCs or clusters were imaged
256 under 5X or 40X magnification respectively. To set up criteria for identifying CTC
257 clusters via images, we analyzed seven single CTCs with intact CK signal distribution
258 and calculated the average nuclei-edge to membrane distance (x). Inter-nuclei-edge
259 distance greater than 2x for any two CTCs were excluded in CTC cluster calling. All
260 measurements were performed in a blind manner. Details of filter and staining are
261 included in the supplementary materials and methods.

262

263 **qRT-PCR**

264 MCF7 and T47D cells were seeded in triplicates into 6-well plates with 120,000 and
265 90,000 cells per well respectively. After desired treatments, RNA was and cDNA was
266 synthesized using iScript kit (#1708890, BioRad, Hercules, CA). qRT-PCR reactions
267 were performed with SybrGreen Supermix (#1726275, BioRad), and the $\Delta\Delta$ Ct method
268 was used to analyze relative mRNA fold changes with *RPLP0* measurements serving as
269 the internal control. All primer sequences can be found in Supplementary Table S10.

270

271 **Immunoblotting**

272 After desired treatments, cells were lysed with RIPA buffer spiked with a fresh protease
273 and phosphatase cocktail (Thermo Scientific, #78442) and sonicated. Protein
274 concentrations were quantified using the Pierce BCA assay kit (Thermo Fisher,
275 #23225). 80-120 μ g of protein for each sample was loaded onto SDS-PAGE gels, and
276 then transferred onto PVDF membranes. The blots were incubated with the following
277 antibodies: desmocollin 1 (sc-398590, RRID: AB_2894905), desmoglein 2 (sc-80663,
278 RRID: AB_2093438), plakophilin (sc-33636, RRID: AB_2164139), connexin 26 (sc-
279 7261, RRID: AB_2110895) and cFOS (sc-52, RRID: AB_2106783) from Santa Cruz;
280 ER- α (#8644, RRID: AB_2617128), HA (#3724, RRID: AB_1549585), Non-phospho- β -
281 catenin (#19807, RRID: AB_2650576), Histone H3 (#4499, RRID: AB_10544537), AIF
282 (#5318, RRID: AB_10634755), GSK3 β (Ser9, #5558, RRID: AB_10013750), phospho-
283 GSK3 α (Ser21, #9316, RRID: AB_659836), GSK3 β (#12456, RRID: AB_2636978) and
284 GSK3 α (#4337, RRID: AB_10859910) from Cell Signaling Technology; β -catenin
285 (#610154, RRID: AB_397555) from BD; Tubulin (T6557, RRID: AB_477584) and
286 connexin 43 (C6219, RRID: AB_476857) from Sigma Aldrich; and *TIMP3* (ab39184,
287 RRID: AB_2204971) from Abcam.

288

289 **IncuCyte Live Cell Imaging System**

290 *Wound scratch assay.* MCF7 or T47D cells were seeded at 150,000 cells/well into
291 Imagelock 96-well plates (Essen Bioscience, #4379) pre-coated with Matrigel (Corning,
292 #356237). Wounds were scratched in the middle of each well using a Wound Maker
293 (Essen Bioscience, #4493). Desired treatments mixed with 5 μ g/ml of proliferation
294 blocker Mitomycin C (Sigma-Aldrich, #10107409001) were loaded after two washes with
295 PBS. The IncuCyte Zoom system was used to record wound images every 4 hours and
296 wound closure density was calculated using the manufacturer's wound scratch assay
297 module. For the dominant negative *TCF4* overexpression experiment, Myc-tagged
298 DNTCF4 plasmids (Addgene, #32729) were transiently transfected into targeted cells
299 for a total of 24 hours before being subjected to the wound scratch assay.

300 *Aggregation rate assay.* 3,000 MCF7 or 4,000 T47D cells were seeded into 96-well
301 round bottom ultra-low attachment plates (Corning, #7007) with 100 μ l of respective

302 media in each well. Cell aggregation was monitored by the IncuCyte living imaging
303 system every hour. Spheroid areas were normalized to time 0.

304

305 **Calcein-labelled cell-cell interaction assay**

306 MCF7 and T47D cells were seeded into black-walled 96 well plate at 150,000 cells per
307 well to achieve a fully confluent monolayer after 24 hours. Separate cultures of cells
308 were digested and labelled with 1 μ M calcein AM (BD Pharmingen, #564061) for 30
309 minutes in room temperature. 40,000 labelled cells were loaded on top of the previously
310 plated monolayers and incubated for 1 hour at 37 $^{\circ}$ C. Cells were washed three times
311 after incubation by manually pouring out the PBS washing agent. The plates were read
312 using Victor X4 plate reader (PerkinElmer) under the excitation and emission
313 wavelength of 485/535nm. Cell-cell adhesion ratios were calculated by dividing the
314 post-wash readouts to the pre-wash readouts after each wash. For the vacuum
315 aspiration method, we used a standard laboratory vacuum pump with a modified speed
316 of approximately 100 ml/minutes. Adhesion ratios after three washes were plotted
317 separately for each independent experiment.

318

319 **ibidi microfluidic system**

320 MCF7 and T47D *ESR1* mutant cells were hormone deprived for 3 days and diluted to
321 10 6 cells in 14ml of respective media before being loaded into the ibidi pump system
322 (ibidi, #10902). Cells were constantly flowing with 15dynes/cm of shear stress for two
323 hours before immediate imaging after being seeded back into a flat bottom ULA plate.
324 For each group, six wells were imaged twice. Time zero (T0) cells were also imaged as
325 the initial time point control. Cell numbers in clusters or non-clusters were manually
326 counted. Cell cluster ratios were calculated by dividing the cell numbers in clusters to
327 the total number of cells. Cell clustering grade was calculated by the cell numbers
328 present in each cluster. For CBX treatment, cells were pre-treated with 100 μ M CBX for
329 two days before being added to the flow chamber. For the desmosome blocking
330 peptides treatment, 75 μ M of each *DSC1*, *DSC2*, *DSG1* and *DSG2* peptide or 150 μ M of
331 each scramble peptide were pre-mixed into cell suspension for flow experiments.

332

333 **Cell-ECM adhesion assay**

334 30,000 cells/well were seeded into collagen I coated (Thermo Fisher Scientific,
335 A1142803) or uncoated 96-well plates. For the ECM array assay, cells were
336 resuspended and loaded into the ECM array plate (EMD Millipore, ECM540). After a 2-
337 hour incubation at 37°C, the plates were washed with PBS three times, and attached
338 cells were quantified using the FluoReporter kit (Thermo Fisher Scientific, F2962).
339 Adhesion ratios were calculated by dividing the remaining cell counts in the washed
340 wells to the initial cell counts in pre-washed plates. For *TIMP3* overexpression, the
341 PRK5M-*TIMP3* plasmid (Addgene, #31715) was transfected into targeted cells, which
342 was subjected to the adhesion assay after a 24-hour transfection period.

343

344 **Chromatin-immunoprecipitation (ChIP)**

345 ChIP experimentation was performed as previously described (23). The
346 immunoprecipitation was performed using ER α (sc543, RRID: AB_631471) and rabbit
347 IgG (sc2027, RRID: AB_737197) antibodies (Santa Cruz Biotechnologies). Histone 3
348 acetylation at K27 site (ab4729, RRID: AB_2218291), and Histone 3 di-methylation at
349 K4 site (ab7766, RRID: AB_2560996) and FOXA1 (ab23738, RRID: AB_2104842)
350 antibodies were obtained from Abcam. Detailed ChIP-seq analysis are provided in the
351 Supplementary Material and Methods.

352

353 **Statistical Analysis**

354 GraphPad Prism software version 7 and R version 3.6.1 were used for statistical
355 analysis. All experimental results included biological replicates and were shown as
356 mean \pm standard deviation, unless otherwise stated. Specific statistical tests were
357 indicated in corresponding figure legends. All tests were conducted as two-tailed, with a
358 $p < 0.05$ considered statistically significant. Drug synergy was calculated based on the
359 Bliss independence model using the SynergyFinder (<https://synergyfinder.fimm.fi/>) (24).
360 Bliss synergy scores were used to determine synergistic effects.

361

362 **Data Availability Statement**

363 The ER and FOXA1 ChIP-seq data has been deposited onto the Gene Expression
364 Omnibus database (GSE125117 and GSE165280). All publicly available resources
365 used in this study are summarized in Supplementary Table S11. All raw data and scripts
366 are available upon request from the corresponding author.

367 **Results**

368 **Significant enrichment of *ESR1* mutations in distant metastases compared to**
369 **local recurrences**

370 We compared *ESR1* mutation frequencies between distant metastatic and locally
371 recurrent tumors. A combination of four previously reported clinical cohorts (MSKCC,
372 METAMORPH, POG570 and IEO) showed that while 155/877 distant metastases (18%)
373 harbored *ESR1* mutations, none were found in 44 local recurrences (Table 1 and
374 Supplementary Table S1) (25-28). To expand upon this observation, we additionally
375 screened 75 ER+ recurrent tumors from the Women's Cancer Research Center
376 (WCRC) and Charite Hospital for *ESR1* hotspot (Y537S/C/N and D538G) mutations
377 using highly sensitive droplet digital PCR (ddPCR). We identified 12 *ESR1* mutation-
378 positive cases among the distant metastases (25%), whereas none of the local
379 recurrences were *ESR1* mutation-positive (Table 1 and Supplementary Table S2).
380 There was no significant difference in time to recurrence for patients with distant vs local
381 recurrences (Supplementary Fig. S1A & Table S3), making it less likely that the
382 observed differences could simply be due to duration of time to recurrence between
383 local and distant recurrences, as was previously suggested (6). If however, we compare
384 time to distant recurrence between tumors with WT and mutant *ESR1*, we observed
385 significantly longer time to recurrence in two of the five cohorts (Supplementary Fig
386 S1B). For three of the cohorts (WCRC/Charite, POG570, and MSKCC), details on lines
387 of therapies was available, and we observed that in two of the cohorts, patients with
388 distant metastases had on average significantly more lines of therapy compared to
389 those with local recurrences (Supplementary Fig. S1C and S1D), and that patients with
390 *ESR1* mutant tumors had been exposed to more lines of therapies than those with WT
391 tumors (Supplementary Fig. S1E). Finally, we repeated our comparative analysis of
392 frequency of *ESR1* mutations in local and distant recurrences restricting it to patients
393 exposed to endocrine therapies and confirmed significant enrichment of *ESR1*
394 mutations in distant metastasis (Supplementary Table S1). Thus, while collectively
395 these analyses recapitulated that *ESR1* mutations are arising primarily as an outcome
396 of therapeutic selection, their more frequent occurrences in distant compared to local

397 recurrences suggest a potential role in promoting metastasis in addition to conferring
398 endocrine resistance.

399 ***ESR1* mutant tumors show a unique transcriptome associated with multiple** 400 **metastatic pathways**

401 To identify candidate functional pathways mediating the metastatic properties of *ESR1*
402 mutant cells, we compared WT and *ESR1* mutant tumor transcriptomes from four
403 cohorts of ER+ metastatic tumors: our local WCRC cohort (46 *ESR1* WT and 8 mutant
404 tumors) (29-31) and three previously reported cohorts - MET500 (34 *ESR1* WT and 12
405 mutants tumors), POG570 (68 *ESR1* WT and 18 mutants tumors) and DFCI (98 *ESR1*
406 WT and 32 mutants tumors) (14,27,32) (Fig. 1A & Supplementary Table S4).

407 Although principal component analyses on global transcriptomes did not segregate
408 *ESR1* WT and mutant tumors (Supplementary Fig. S2A), both “Estrogen Response
409 Early” and “Estrogen Response Late” signatures were significantly enriched in *ESR1*
410 mutant tumors in 3 out of 4 cohorts, with a trend towards enrichment in the fourth cohort
411 (Fig. 1B). These results recapitulate the observation of ER hyperactivation as a result of
412 hotspot mutations, previously described in other preclinical studies (12,14,20).

413 Differential gene expression analysis identified a considerable number of altered genes
414 that were associated with *ESR1* mutations (Fig. 1C & Supplementary Table S5), which
415 further inferred functional alterations in various metastasis-related pathways.

416 Remarkably, “Cell-To-Cell Signaling & Interaction” and “Cell Movement” were featured
417 among the top five altered pathways for *ESR1* mutant tumors in all four cohorts (Fig.
418 1D).

419 In addition to the broad effects associated with *ESR1* mutations, we next questioned
420 whether different *ESR1* mutant variants could display divergent functions. A meta-
421 analysis of the five above-mentioned ER+ MBC cohorts examining *ESR1* mutations
422 underscored D538G (37%) and Y537S (24%) as the predominant variants (Fig. 1E).
423 Given the challenge of merging RNA-seq data sets from multiple cohorts due to
424 immense technical variations, we selectively compared mutation variant specific
425 transcriptomes of ten Y537S- or eight D538G-harboring tumors to the WT counterpart

426 (n=32) respectively from the DFCI cohort, which provided the largest numbers and thus
427 maximized statistical power. Aligning enrichment levels of 50 hallmark gene sets for the
428 two mutant variants again confirmed “Estrogen Response Early” and “Estrogen
429 Response Late” as the top co-upregulated pathways (Fig. 1F), with Y537S tumors
430 displaying higher ER activation (Supplementary Fig. S2B), consistent with cell line
431 studies (12,33). The similar observation was also validated in MET500 and POG570
432 cohort regardless of the smaller sample size (Supplementary Fig. S2B). We also
433 identified enriched cell cycle related pathways (E2F targets, G2M checkpoint and mitotic
434 spindle) and metabolic related pathways (fatty acid, bile acid and xenobiotic
435 metabolisms) in Y537S and D538G tumors, respectively, implying that different *ESR1*
436 mutant variants might hijack distinct cellular functions to promote malignancy. Again,
437 similar trends of these mutant-variant pathways were recapitulated in POG570 cohort
438 (Supplementary Fig. S2C). Taken together, these results provide support that despite
439 mutant variant-specific alterations, *ESR1* mutations might broadly mediate metastatic
440 phenotypes through effects on cell-to-cell interactions and cell movement. We next
441 validated the *in silico* results using previously established genome-edited MCF7 and
442 T47D cell line models (12).

443 ***ESR1* mutant-cells exhibit stronger cell-cell adhesion**

444 We first addressed the enrichment of cell-cell interaction signaling in the mutant tumors
445 through morphological inspection of cell cluster formation in suspension culture (Fig.
446 2A). We observed more compact cell clusters in MCF7 and T47D mutant cell lines
447 compared to their WT counterparts after six days of suspension culture. A time course
448 study confirmed enhanced cluster formation 24-48hrs past cell seeding (Supplementary
449 Fig. S3A). Similar observations were made in individual clones, eliminating the
450 possibility for clonal effects (Supplementary Fig. S3B).

451 Since *ESR1* mutant cells displayed significantly increased ligand-independent growth in
452 suspension (Fig. 2B), we sought to rule out the possibility that increased cluster
453 formation was simply a result of increased cell number by assessing cell-cell adhesive
454 capacity using multiple approaches in short term culture (within 1 day). We therefore

455 directly quantified homotypic cell-cell interactions by measuring the adhesion of calcein-
456 labelled *ESR1* WT or mutant cells. This assay showed that both MCF7 mutant cells
457 exhibited significantly stronger cell-cell adhesion compared to the WT cells (Fig. 2C). In
458 T47D cells, a similar effect was observed, but was limited to the T47D-Y537S mutant
459 cells (Supplementary Fig. S4A). These assays were complemented by quantification of
460 cell aggregation rates as a direct reflection of cell-cell adhesion, which confirmed faster
461 aggregation in MCF7-Y537S/D538G and T47D-Y537S cells (Fig. 2D & Supplementary
462 Fig. S4B-S4D). In addition, these stronger cell-cell adhesive properties were also
463 reproduced in additional *ESR1* mutant cell models from other laboratories (19,20)
464 (Supplementary Fig. S4E and S4F).

465 Cell-cell interaction has been reported to affect several stages of metastasis, including
466 collective invasion, intravasation, dissemination and circulation (34-36). To test whether
467 ER mutations may affect tumor cell-cell adhesion in circulation, we utilized a microfluidic
468 pump system to mimic arterial shear stress. Comparing representative images before
469 and after 2 hours of microfluidic flow, we found MCF7 *ESR1* mutant cells had a greater
470 tendency to aggregate together (Fig. 2E and 2F). Larger clusters comprised of five or
471 greater cells were more prevalent in the *ESR1* mutant cell lines, whereas smaller two-
472 cell clusters were diminished (Fig. 2G). A similar phenotype was also identified in
473 additional MCF7 *ESR1* mutant cells and in our T47D-Y537S cell line (Supplementary
474 Fig. S5A-S5I), consistent with our observations in static conditions. In an additional
475 orthogonal approach, we utilized a quantitative microfluidic fluorescence microscope
476 system simulating blood flow (37). Quantification of dynamic adhesion events
477 normalized to adhesion surfaces revealed a consistent enhanced cell-cell adhesion
478 capacity of *ESR1* mutant MCF7 cells (Supplementary Fig. S5J-S5K, Supplementary
479 videos 1-3). Together, these results show that hotspot *ESR1* mutations confer
480 increased cell-cell attachment under static and fluidic conditions, and that the effect size
481 is dependent upon mutation type and genetic backgrounds. These findings are at odds
482 with increased EMT features (18), and indeed the majority of *ESR1* mutant models and
483 tumors did not show increased EMT signature or increased expression of EMT marker
484 genes (Supplementary Fig. S6A-S6D).

485 We next sought to assess whether this unexpected phenotype translated into numbers
486 of CTC clusters and subsequent metastasis *in vivo*. One hour post intracardiac injection
487 into athymic mice, circulating MCF7 WT and mutant cells were enriched from blood
488 using a previously described electrical CTC filtering method (38) (Fig. 2H). 41%-81% of
489 CTC clusters were composed of both cancer and non-cancer cells (Supplementary Fig.
490 S7A). Despite no difference in the average amount of single CTCs and CTC clusters
491 per mouse between the WT and mutant *ESR1* (Supplementary Fig. S7B & S7C), we
492 found that overall MCF7-Y537S mutant cells were significantly enriched in clusters with
493 greater than 2 cells (Fig. 2I). Furthermore, quantification of inter-nuclei distances
494 between two-cell clusters revealed denser MCF7-Y537S clusters (Fig. 2J), supporting
495 stronger MCF7-Y537S cell-cell interactions in an *in vivo* blood circulation environment.
496 The data from the MCF7-D538G mutant cells did not recapitulate the adhesive
497 phenotype we discerned *in vitro*, suggesting mutation site-specific interactions with the
498 *in vivo* microenvironment potentially affect cluster formation.

499 We next performed tail vein injection and monitored bloodborne metastatic development
500 in longer-term *in vivo* experiments without estradiol supplement (Fig. 2K). We observed
501 multiple distant macro-metastatic tumors in 4/6 (67%) MCF7-Y537S mutant cell-injected
502 mice (Fig. 2L), likely as an outcome of the well-established ligand-independent cell
503 growth. In contrast, distant macro-metastatic tumor was observed in only one mouse of
504 MCF7-D538G group (1/7) and none in MCF7-WT group (0/7) (Fig. 2M, left panel). The
505 enhanced macro-metastasis observed in MCF7-Y537S but not D538G mutant was
506 consistent with our *in vivo* CTC clustering experiment, opening up the possibility that the
507 enhanced CTC clustering ability might confer an additional metastatic advantage. We
508 detected no difference in lung micro-metastatic foci areas between WT and mutant cell-
509 injected mice, potentially due to a high baseline of MCF7 lung colonization capacity
510 (Fig. 2M, right panel). In contrast to our results with MCF7 cells, we only discerned one
511 macro-metastatic tumor from each T47D mutant group (Y537S: 1/6; D538G: 1/7) and
512 none in T47D-WT group (0/7) after 23 weeks of injection (Fig. 2O, left panel),
513 underpinning its less aggressive behavior as compared to MCF7 cells (39,40).
514 However, both T47D-Y537S and T47D-D538G mutant cells resulted in enlarged lung
515 micro-metastases (Fig. 2N and 2O, right panel).

516 Encouraged by our *in vitro* and *in vivo* findings, we next examined CTC clusters in
517 patients with *ESR1* mutant tumors. Taking advantage of a recent CTC sequencing
518 study (41), we sought to generate CTC cluster gene signatures. Differential gene
519 expression analysis in two patients with ER+ disease who had at least two CTC clusters
520 and single CTCs sequenced identified CTC cluster enriched genes (Supplementary Fig.
521 S8A and Table S6), which we subsequently applied to our RNA-seq dataset with 51
522 pairs of ER+ primary-matched metastatic tumors (44 *ESR1* WT and 7 mutant) merged
523 from the WCRC and DFCI cohorts. *ESR1* mutant metastatic tumors exhibited
524 significantly higher enrichment of CTC cluster-derived gene signatures (Supplementary
525 Fig. S8B and S8C).

526 To examine the interplay between *ESR1* mutations, numbers of CTCs, and clinical
527 outcome, we analyzed a cohort of 151 patients with MBC. Median age at the first blood
528 draw for CTCs enumeration was 55 years (IQR: 44 - 63 years), 76 patients (50.3%)
529 were diagnosed with ER+ HER2-negative MBC, 38 (25.2%) with HER2-positive MBC
530 and 37 (24.5%) with TNBC. Bone (49.7%), lymph nodes (41.1%), lung (34.4%) and liver
531 (34%) were the most common sites of metastasis (Supplementary Table S7). Median
532 number of CTCs was 1 (IQR: 0-10), clusters were detectable in 14 patients (9.3%) (Fig.
533 2P) and in this subgroup the median number of clustered CTCs (i.e., number of CTCs
534 involved in clusters) was 15.5 (IQR: 4 - 20). Clusters with CTCs >4 and ≤4 were
535 detected in 10 (6.6 %), and 4 (2.7%) cases, respectively. Among patients without
536 clusters (90.7%), 101 (66.89%) and 36 (23.84%) were respectively classified as stage
537 IV Indolent (< 5 CTCs) and Aggressive (≥ 5 CTCs) according to our previous study (42)
538 (Supplementary Table S7). Mutations in hotspots D538 and Y537 of *ESR1* were
539 detected in 30 patients (19.9%), while mutations in hotspots E453 and H1047 of
540 PIK3CA were detected in 40 patients (26.5%) (Supplementary Table S7). Median
541 follow-up was 30.8 months. A significant association was observed between *ESR1*
542 genotype status and clustered CTCs > 4 ($P = 0.029$) (Fig. 2Q), a significant association
543 was retained after adjusting for MBC subtype (OR: 5.51, 95%C.I.: 1.29 - 23.52 $P =$
544 0.021). A similar trend was highlighted in the ER+ HER2-negative subgroup specifically
545 (Supplementary Fig. S8D). No association was observed with respect to PIK3CA
546 ($P=0.725$). Notably, patients with > 4 clustered CTCs experienced the worse prognosis

547 with respect to Stage IV indolent in terms of OS both in the general population (Fig. 2R)
548 ($P < 0.0001$) and in the ER+ HER2-negative subgroup (Supplementary Fig. S8E) ($P <$
549 0.0001). After adjusting for MBC subtype, >4 clustered CTCs and Stage IV aggressive
550 without clusters retained their prognostic impact (respectively HR: 15.50, 95%CI: 6.90 -
551 34.82. $P < 0.001$; HR: 2.37, 95%CI: 1.38 - 4.06. $P = 0.002$).

552 **Mutant *ESR1* cells show increased desmosome gene and gap junction gene** 553 **families**

554 To elucidate the mechanism of enhanced cell-cell adhesion, we investigated the
555 enrichment of four major cell-cell junction subtypes – desmosomes, gap junctions
556 (connexons), tight junctions and adherens junctions within the cell model RNA-seq data
557 (12) (Supplementary Table S6). Enrichment of the desmosome gene and gap junction
558 gene families was observed in both MCF7-Y537S/D538G and T47D-Y537S cells (Fig.
559 3A). Tight junctions were enriched in WT cells, and there were no differences in the
560 adherens junction gene family expression (Supplementary Fig. S9A). Individual gene
561 expression analysis ($FC > 1.2$, $p < 0.05$) identified 18 commonly upregulated desmosome
562 genes and 4 gap junction genes in both MCF7 *ESR1* mutant cell lines (Fig. 3B). In
563 addition to keratins, induction of classical desmosome genes *DSC1/2*, *DSG1/2* and
564 *PKP1*, and gap junction genes *GJA1*, *GJB2* and *GJB5* were observed and validated by
565 qRT-PCR in MCF7 cells (Fig. 3D). Higher protein levels were also observed for *DSC1*,
566 *DSG2*, *PKP1*, *GJA1* (Cx43), and *GJB2* (Cx26) (Fig. 3C). Immunofluorescence staining
567 revealed significantly higher *DSG2* expression in MCF7-Y537S at cell-cell contact
568 surfaces, with a trend observed in MCF7-D538G (Fig. 3E). Consistent with the weaker
569 *in vitro* cell-cell adhesion phenotypes in T47D mutant cells, we observed less
570 pronounced desmosome and gap junction gene expression changes in T47D-Y537S
571 cells (Supplementary Fig. S9B). We validated the overexpression of the key
572 desmosome and gap junction genes in RNA-seq datasets from seven additional *ESR1*
573 mutant cell models and performed further validation studies in two of them
574 (Supplementary Fig. S9C-S9E) (11,15,19). Moreover, mining RNA-seq data from
575 recently reported *ESR1* WT and mutant *ex vivo* CTC models (43), we observed
576 overexpression of three gap junction and desmosome genes in the *ESR1* mutant CTC

577 lines (Supplementary Fig. S9F). Finally, the top upregulated desmosome and gap
578 junction genes (Supplementary Table S6) were also found significantly enriched in intra-
579 patient matched primary and metastatic lesions with *ESR1* mutations (Fig. 3F).

580 We next investigated the functional roles of the reprogrammed adhesome in the *ESR1*
581 mutant MCF7 cells. Transient individual knockdown of *DSC1*, *DSC2*, *GJA1* or *GJB2* did
582 not cause significant changes in adhesion in either *ESR1* mutant line (Supplementary
583 Fig. S10A). However, we found compensatory effects observed in the desmosome and
584 gap junction knockdowns as exemplified by increased *GJA1* levels after *DSC1* or *DSC2*
585 knockdown (Supplementary Fig. S10B). The adhesive phenotype was disrupted,
586 however, with an irreversible pan-gap junction inhibitor, Carbenoxolone (CBX), or with
587 blocking peptide cocktails against desmocollin1/2 and desmoglein1/2 proteins. Both
588 treatments caused significant inhibition of cell-cell aggregation in static conditions
589 (Supplementary Fig. S10C & S10D) as well as diminished cluster propensities and size
590 in microfluidic conditions (Fig. 3G-3L), suggesting redundancy in the mutant-driven
591 reprogrammed desmosome and connexon pathways. In summary, MCF7-
592 Y537S/D538G and T47D-Y537S mutants showed increased expression of desmosome
593 and gap junction gene family components, which contributes to our observed enhanced
594 cell-cell adhesion phenotype.

595 We next investigated the mechanisms underlying the elevated desmosome and gap
596 junction components in *ESR1* mutant cells. Because hotspot *ESR1* LBD mutations are
597 well-described as conferring constitutive ER activation, we first examined if these cell-
598 cell adhesion target genes are direct outcomes of ligand-independent transcriptional
599 programming. Interrogating publicly available RNA-seq and microarray datasets of six
600 estrogen treated ER+ breast cancer cell lines (12,23,44,45), we found limited and
601 inconsistent E2 induction of all examined cell-cell adhesion genes when compared to
602 classical E2 downstream targets such as *GREB1* and *TFF1* (Supplementary Fig. S11A).
603 Surprisingly, mining our MCF7 *ESR1* mutant cell model ER ChIP-seq data (46) showed
604 an absence of proximate Y537S or D538G mutant ER binding sites (\pm 50kb of TSS) at
605 desmosome and connexon target gene loci. These results suggest that the

606 reprogrammed cell-cell adhesion is not a direct consequence of mutant ER genomic
607 binding.

608 We therefore hypothesized that these altered adhesion target genes might be regulated
609 via a secondary downstream effect of the hyperactive mutant ER. A seven-day siRNA
610 ER knockdown assessment identified *GJA1* as the only target gene that could be
611 blocked in mutant cells following ER depletion, whereas, strikingly, *DSC1*, *DSG1*, *GJB2*
612 and *GJB5* mRNA levels were increased in all cell lines (Fig. 3M). This was congruent
613 with *ESR1* knockdown in five additional ER+ parental cell lines, with the majority
614 exhibiting a decrease in *GJA1* expression levels (Supplementary Fig. S11B). To unravel
615 potential intermediate transcription factors (TFs) involved in the secondary regulation,
616 we examined the levels of TFs previously reported to regulate *GJA1* expression (47)
617 (Supplementary Fig. S11C). Among those, the AP1 family component *FOS* (cFos) was
618 identified as the top TF upregulated in *ESR1* mutant cells in a ligand-independent
619 manner. In addition, the AP1-associated transcriptional signature was also significantly
620 enriched in MCF7 *ESR1* mutant cells (Supplementary Fig. S11D), and hence we tested
621 if *GJA1* overexpression was dependent on the cFOS/AP1 transcriptional network.
622 Higher cFOS mRNA and protein levels in *ESR1* mutant cells were confirmed, which
623 declined along with *GJA1* levels after *ESR1* knockdown (Fig. 3N & Supplementary Fig.
624 S11E). Importantly, pharmacological inhibition of cFOS-DNA binding partially rescued
625 *GJA1* overexpression in *ESR1* mutant cells (Fig. 3O, Supplementary Fig. S11F-S11G).
626 In conclusion, our results denote *GJA1* as an indirect target of mutant ER through
627 activation of the cFOS/AP1 transcriptional axis in MCF7 cell models.

628 Since the majority of the cell-cell adhesion targets altered in the *ESR1* mutant cells
629 were not direct ER target genes (Supplementary Fig. S11A & S11B), we investigated
630 potential impacts of epigenetic remodeling on these targets. Using our recently reported
631 ATAC-seq dataset from T47D *ESR1* mutant cells (19), we observed that one of the
632 connexon targets, *GJB5*, exhibited increased chromatin accessibility at its gene locus in
633 T47D-Y537S cells (Supplementary Fig. S12A & S12B), suggesting that epigenetic
634 activation modulates gene expression in this particular context. We further evaluated
635 active histone modifications on our target gene loci in the MCF7 model. We observed

636 enhanced H3K27ac and H3K4me2 recruitment in both MCF7-Y537S and D538G cells
637 at the nearest two histone modification sites around the *DSC1* and *DSG1* loci, the two
638 most upregulated desmosome component genes in MCF7 mutant cells (Fig. 3P),
639 suggesting activation of desmosome genes via an indirect ER-mediated epigenetic
640 activation (Fig. 3Q).

641 ***ESR1* mutations promote reduced adhesive and enhanced invasive properties via**
642 **altered *TIMP3*-MMP axis**

643 In addition to altered cell-cell adhesion, metastasis is also mediated by coordinated
644 changes in cell-matrix interaction (48,49). Therefore, we assessed whether mutant ER
645 affects interaction with the extracellular matrix (ECM). Computational analysis showed
646 inverse correlation between ECM receptor pathway signatures and *ESR1* mutation
647 status in the DFCI cohort with the same trend appearing in 2/3 of the remaining cohorts
648 (Fig. 4A, Supplementary Fig. S13A & Table S6). Employing an adhesion array on seven
649 major ECM components, we observed that the MCF7 *ESR1* mutant cell lines
650 consistently lacked adhesive properties on almost all ECM components with the
651 exception of fibronectin, and T47D *ESR1* mutant cells displayed reduced adhesion on
652 collagen I, collagen II and fibronectin (Fig. 4B). Considering that collagen I is the most
653 abundant ECM component in ER+ breast cancer (Supplementary Fig. S13B), we
654 repeated the adhesion assay on collagen I (Fig. 4C & 4D; Supplementary Fig. S13C &
655 S13D) and similarly found reduced adhesion in both ER mutant cells. In an orthogonal
656 approach, we visualized and quantified adhesion in a co-culture assay on collagen I
657 using differentially labelled *ESR1* WT and mutant cells, which confirmed significantly
658 decreased adhesive properties in the mutant cells (Supplementary Figure S13E &
659 S13F). Of note, *ESR1* mutant adhesion deficiency on collagen I was also observed in
660 two additional *ESR1* mutant models (Supplementary Fig. S13G).

661 We sought to investigate the molecular mechanisms underlying the unique defect of
662 collagen I adhesion in *ESR1* mutant cells. There was no consistent change in
663 expression of members of the integrin gene family, encoding well-characterized direct
664 collagen I adhesion receptors, in our cell line models (Supplementary Fig. S14A and

665 Supplementary Table S6). We therefore hypothesized that another gene critical in
666 regulation of ECM genes might be altered and to test this directly, we performed gene
667 expression analysis of 84 ECM adhesion-related genes using a qRT-PCR array
668 (Supplementary Table S8). Pairwise comparisons between each mutant cell line and
669 corresponding WT cells revealed a strong context-dependent pattern of ECM network
670 reprogramming, with more pronounced effects in MCF7 cells (Fig. 4E). Intersection
671 between Y537S and D538G mutants showed 23 and 1 consistently altered genes in
672 MCF7 and T47D cells, respectively (Fig. 4F). *TIMP3*, the gene encoding tissue
673 metalloproteinase inhibitor 3, was the only shared gene between all four mutant cell
674 models (Fig. 4F), and we confirmed its decreased expression at the mRNA (Fig. 4G &
675 Supplementary Fig. S14B) and protein level (Fig. 4H), as well as in other genome-
676 edited *ESR1* mutant models (Supplementary Fig. S14C). E2 treatment represses
677 *TIMP3* expression, suggesting that its downregulation in *ESR1* mutant cells is likely due
678 to ligand-independent repressive ER activity (Supplementary Fig. S14C).
679 Downregulation of *TIMP3* was found in several (but not all) tamoxifen resistant MCF7
680 models, but long-term estradiol deprived (LTED) MCF7 showed upregulation
681 (Supplementary Fig. S14D). Further, changes in *TIMP3* were not seen in other LTED
682 models, suggesting that alteration of *TIMP3* by mutant *ESR1* is complex and warrants
683 further investigation. Overexpression of *TIMP3* rescued the adhesion defect in *ESR1*
684 mutant cells (Figure 4I, 4J & Supplementary Fig. S14E), with no impact on cell
685 proliferation (Supplementary Fig. S14F). Collectively, these data imply a selective role
686 for *TIMP3* downregulation in causing the decreased cell-matrix adhesion phenotype of
687 the *ESR1* mutant cells, consistent with a critical role for *TIMP3* in metastasis in other
688 cancer types (50,51).

689 Given the role of *TIMP3* as an essential negative regulator of matrix metalloproteinase
690 (MMP) activity, we compared MMP activity between *ESR1* WT and mutant cells. A pan-
691 MMP enzymatic activity assay revealed significantly increased MMP activation in all
692 mutant cells (Fig. 4K & 4L), indicating that the *ESR1* mutant cells have increased
693 capacity for matrix digestion. This was validated in spheroid-based invasion assays in
694 which cells were embedded in collagen I (Fig. 4M) but without notable growth
695 differences (Supplementary Fig. S15A & S15B). This was additionally visualized in co-

696 culture spheroid invasion assays using differentially labelled T47D *ESR1* WT and
697 mutant cells, which showed an enrichment of *ESR1* mutant cells at the leading edge of
698 the spheroids (Supplementary Fig. S15C). Lastly, we tested if MMP blockade could
699 repress *ESR1* mutant-modulated invasive and adhesive alterations. Marimastat
700 treatment substantially reduced the invasive phenotype of *ESR1* mutant cells without
701 inhibiting growth (Fig. 4N, 4O & Supplementary Fig. S15D). Furthermore, the reduced
702 adhesive property was rescued by Marimastat treatment in *ESR1* mutant cells
703 (Supplementary Fig. S15E). These data demonstrate that decreased TIMP3 expression,
704 resulting in increased MMP activation causes enhanced matrix digestion associated
705 with decreased adhesion to ECM, ultimately conferring invasive properties to *ESR1*
706 mutant cells.

707 ***De novo* FOXA1-mediated Wnt pathway activation enhances of the T47D-D538G** 708 **cell migration**

709 T47D D538G cells showed increased *in vivo* tumorigenesis despite showing less
710 pronounced adhesive phenotypes compared to T47D Y537S and MCF7 Y537S/D538G
711 cells. Reasoning mutation and context-dependent metastatic activities of the mutant ER
712 protein and having identified “Cellular Movement” as another top hit in our initial
713 pathway analysis of differentially expressed genes in *ESR1* mutant tumors (Fig. 1D), we
714 assessed potential differences in cellular migration between the different models.
715 Wound scratch assays identified significantly increased cell motility in the T47D-D538G
716 model (Fig. 5A & 5B), but not in T47D-Y537S (Fig. 5B) or MCF7 mutant cells
717 (Supplementary Fig. S16A & S16B). This enhanced motility was shared between the
718 three individual T47D-D538G clones again excluding potential clonal artifacts
719 (Supplementary Fig. S16C & S16D). Furthermore, we observed a different morphology
720 of T47D-D538G cells at the migratory leading edges (Fig. 5C) further confirmed by
721 larger and stronger assembly of F-actin filaments at the edge of T47D-D538G cell
722 clusters (Supplementary Fig. S16E-S16H). To mimic collective migration from a cluster
723 of cells, we utilized a spheroid-based collective migration assay on type I collagen (Fig.
724 5D). The distance to the leading edges of T47D-D538G mutant cells was significantly
725 longer compared to WT spheroids (Fig. 5E). In orthogonal approaches, enhanced

726 migratory capacities of T47D-D538G cells were observed in co-culture assay using
727 labelled T47D-WT and D538G cells (Supplementary Fig. S16I & S16J) and in Boyden
728 chamber transwell assays (Supplementary Fig. S16K & S16L). Finally, in T47D
729 overexpression models, we also observed significantly enhanced migration in D538G
730 compared to WT overexpressing cells (Supplementary Fig. S17A-S17E).

731 To understand the mechanisms underlying the migratory phenotype of T47D-D538G
732 cells we identified pathways uniquely enriched in these cells. GSEA identified endocrine
733 resistance-promoting pathways (e.g. E2F targets) in both T47D mutants, whereas Wnt-
734 β -catenin signaling was one of the uniquely enriched pathways in T47D-D538G (Fig.
735 5F). Hyperactivation of the canonical Wnt- β -catenin pathway was further confirmed by a
736 Top-Flash luciferase assay (Supplementary Fig. S18A). We also observed increased
737 phosphorylation of GSK3 β and GSK3 α as well as β -catenin (both total and nuclear)
738 protein levels in T47D-D538G cells (Fig. 5G, Supplementary Fig. S18B and S18C).
739 Stimulation of T47D-WT cells with Wnt3A was not able to increase the migration to the
740 same level of D538G cells (Supplementary Fig. S18D), suggesting that Wnt activation is
741 a required but not sufficient factor in driving this phenotype. To address the potential
742 clinical relevance of these findings, we utilized the porcupine inhibitor LGK974, which
743 prevents the secretion of Wnt ligands and is currently being tested in a clinical trial for
744 patients with advanced solid tumors including breast cancer (NCT01351103) (52,53).
745 Treatment with LGK974 resulted in a 20% and 40% inhibition of T47D *ESR1* WT and
746 D538G mutant cell migration respectively (Fig. 5H and Supplementary Fig. S18E) yet
747 had no effect on cell proliferation (Supplementary Fig. S18F). We next studied the
748 combination of LGK974 and the selective ER degrader (SERD), Fulvestrant, in
749 migration assays, in which we detected significant synergy (Fig. 5I), suggesting that
750 combination therapy co-targeting the Wnt and ER signaling pathways might reduce the
751 metastatic phenotypes of Wnt hyperactive *ESR1* mutant tumors.

752 We sought to decipher the mechanisms underlying T47D-D538G Wnt hyperactivation.
753 First, a set of Wnt component genes were identified to be uniquely enriched in tumors
754 with D538G but not other mutant variants in the DFCI cohort (Supplementary Fig.
755 S18G). Comparing the fold changes of canonical Wnt signaling positive regulators

756 between T47D-Y537S and T47D-D538G mutant cells, we identified eight candidate
757 genes exhibiting pronounced enrichment in T47D-D538G cells (Fig. 5J), including
758 ligands (e.g. *WNT6A*), receptors (e.g. *LRP5*) and transcriptional factors (e.g. *TCF4*).
759 With the exception of *LRP5*, none of these candidate genes were induced by E2
760 stimulation in T47D *ESR1* WT cells (Supplementary Fig. S19A). Lack of consistent E2
761 regulation was confirmed in five additional ER+ breast cancer cell lines (Supplementary
762 Fig. S19B). Hence, we alternatively hypothesized that D538G ER might gain *de novo*
763 binding sites proximal to Wnt pathway genes allowing their induction. We mapped ER
764 binding globally by analyzing ER ChIP-sequencing in T47D WT and *ESR1* mutant cells.
765 Consistent with previous studies (14,20), mutant ER were recruited to binding sites
766 irrespective of hormone stimulation (Supplementary Fig. S19C & Table S9). However,
767 none of the mutant ER bound regions mapped to identified Wnt pathway genes (\pm 50kb
768 of TSS), again suggesting a lack of direct canonical ER regulation. Moreover, short-term
769 fulvestrant treatment only weakly dampened T47D-D538G cell migration (Fig. 5K & 5M)
770 suggesting that ER activation may not be an essential prerequisite for enhanced cell
771 migration in D538G cells.

772 Given our recent findings of enriched FOXA1 motifs in gained open chromatin of T47D-
773 D538G cells (19), we decided to validate this pivotal *in silico* prediction, focusing on our
774 observed migratory phenotype. In contrast to the limited effects of ER depletion,
775 strikingly, FOXA1 knockdown fully rescued the enhanced migration in T47D-D538G
776 cells (Fig. 5L & 5N), indicating a more dominant role of FOXA1 in controlling T47D-
777 D538G cell migration. Ligand-independent 2D growth of T47D-D538G cells was
778 inhibited by both fulvestrant and FOXA1 knockdown (Supplementary Fig. S19D),
779 suggesting a canonical ER-FOXA1 co-regulatory mechanism in growth, distinguished
780 from the role of FOXA1 in the regulation of migration.

781 To further explore how FOXA1 contributes to the migratory phenotype, we performed
782 FOXA1 ChIP-sequencing to decipher the genomic binding profiles. We identified
783 approximately 30,000 peaks in T47D WT cells regardless of E2 stimulation and a ~1.6
784 fold increase in binding sites of the Y537S (61,934) and D538G (54,766) ER mutants
785 (Supplementary Fig. S20A & Supplementary Table S9). PCA distinctly segregated all

786 four groups (Fig. 5O), suggesting unique FOXA1 binding site redistribution. Comparison
787 of binding intensities revealed 14%, 28% and 21% FOXA1 binding sites were altered in
788 WT+E2, Y537S and D538G groups, respectively, with a predominant gain of binding
789 intensities in the two T47D mutants (Fig. 5P and Supplementary Fig. S20B).

790 Since FOXA1 is a well-known essential pioneer factor of ER in breast cancer, we
791 examined interplay between FOXA1 and WT and mutant ER. Interestingly, both Y537S
792 (39%) and D538G (25%) ER binding sites showed a significantly lower overlap between
793 FOXA1 compared to the WT+E2 group (56%), albeit with the increased number of
794 gained mutant FOXA1 binding sites (Supplementary Fig. S20C). This discrepancy
795 suggests that FOXA1 exhibits a diminished ER pioneering function and instead might
796 contribute to novel functions via gained *de novo* binding sites. Co-occupancy analysis
797 using isogenic ATAC-seq data (19) uncovered that the open chromatin of T47D-D538G
798 cells was more associated with FOXA1 binding sites compared to WT and T47D-Y537S
799 cells (Fig. 5Q). FOXA1 binding intensities were also stronger in D538G ATAC-sites
800 (Supplementary Fig. S20D). Collectively, these results provide evidence that FOXA1
801 likely plays a critical role in the D538G mutant cell to reshape its accessible genomic
802 landscape.

803 We further investigated the impact of the gained FOXA1-associated open chromatin on
804 transcriptomes, particularly exploring *ESR1* mutant-specific genes. Intersection of the
805 gained FOXA1- and ATAC-sites for annotated T47D-D538G genes with non-canonical
806 ligand-independence identified 25 potential targets that could be attributed to *de novo*
807 FOXA1 bound open chromatin, exemplified by *PRKG1* and *GRFA* as top targets (Fig.
808 5R & Supplementary Fig. S21A). Notably, one of our identified D538G specific Wnt
809 regulator genes, *TCF4*, was uncovered in this analysis. Higher *TCF4* expression in
810 T47D-D538G cells was validated by qRT-PCR and furthermore this increased
811 expression could be fully blocked following FOXA1 knockdown (Supplementary Fig.
812 S21B). Additionally, stronger FOXA1 recruitment at the *TCF4* gene locus was validated
813 via CHIP-qPCR (Supplementary Fig. S21C and S21D). Importantly, overexpression of
814 dominant negative *TCF4* strongly impaired cell migration in T47D-D538G, while it only
815 slightly affected WT cells (Fig. 5S). Together, these results support that FOXA1 binding

816 site redistribution leads to novel chromatin remodeling and enhanced expression of
817 genes with roles in metastases including *TCF4*, which subsequently activate Wnt-driven
818 migration in T47D-D538G cells.

819

820 Discussion

821 Hotspot somatic mutations clustered in the LBD of ER represent a prevalent molecular
822 mechanism that drives antiestrogen resistance in ~30% of advanced ER+ breast
823 cancer. There is an urgent need for a deeper understanding of this resistance
824 mechanism in order to develop novel and personalized therapeutics. Utilizing clinical
825 samples, *in silico* analysis of large datasets, and robust and reproducible
826 experimentation in multiple genome-edited cell line models, our study uncovers complex
827 and context-dependent mechanisms of how *ESR1* mutations confer gain-of-function
828 metastatic properties. We identified *ESR1* mutations as multimodal metastatic
829 modulators hijacking adhesive and migratory networks, and thus likely influencing
830 metastatic pathogenesis and progression. Mechanistically, we uncovered novel ER-
831 indirect regulation of metastatic candidate gene expression, distinct from previously
832 described (11,12,54) canonical ligand-independent gene induction. Nonetheless, some
833 limitations were noted in our study, such as the lack of *in vivo* validation of studied
834 therapeutic approaches and lack of proposed target validation in clinical specimens. In
835 addition, our numbers for clinical samples of paired primary-metastatic tumors harboring
836 *ESR1* mutations is finite, necessitating validation in future studies with larger clinical
837 cohorts.

838 We discovered enhanced cell-cell adhesion via upregulated desmosome and gap
839 junction networks in cell lines and clinical samples with *ESR1* mutations. These
840 transcriptional alterations are associated with a specific clinical phenotype characterized
841 not only by treatment resistance, but also by high CTC count and a different metastatic
842 organotropism (55,56). We propose that this key alteration may support increased
843 metastases in ER mutant tumors through facilitating the formation of homo- or
844 heterotypic CTC clusters, providing a favorable environment for CTC dissemination, as
845 previously described (34). This idea is further supported by previous data showing
846 upregulation of the desmosome gene plakoglobin (*JUP*) which may play a role in a CTC
847 cluster formation signature (34). We observed increased expression of plakophilin,
848 desmocollin, and desmoglein in *ESR1* mutant cells, suggesting the importance of the
849 broad desmosome network reprogramming for functional cell clustering activity.

850 Moreover, enhanced gap junction genes might potentiate intercellular calcium signaling,
851 facilitating the prolonged survival of various metastatic cell types tethered to *ESR1*
852 mutant cells *en route* (57). Dissociation of CTC cluster using Na⁺/K⁺ ATPase inhibitors
853 decreased metastasis *in vivo* (41). In addition, previous studies have validated the anti-
854 tumor effects of FDA-approved gap junction blockers carbenoxolone *in vivo* (58). Our
855 results warrant additional preclinical studies using drugs targeting desmosome and gap
856 junctions, with the ultimate goal of applying these treatments in a CTC-targeted clinical
857 trial to improve outcomes for patients harboring breast cancers with *ESR1* mutations.

858 Previous studies using similar *ESR1* mutant cell models described enhanced migratory
859 properties (15,16), but no mechanistic explanations were uncovered. Here we identify a
860 critical role for Wnt- β -catenin signaling and show that co-targeting of Wnt and ER
861 resulted in synergistic inhibition of cell migration. Intriguingly, the strong effect we
862 observed on migration was unique to T47D-D538G cells, a discovery that was made
863 possible through our use of multiple genome-edited mutation models. This finding might
864 help explain the higher frequency of D538G mutations in metastatic samples, despite
865 the stronger endocrine resistance phenotype of Y537S mutation (5,12,14,33). Markedly,
866 although we highlighted the up-regulation of TCF4 as an outcome of de novo FOXA1
867 reprogramming, it is plausible that other increased Wnt regulators including receptors
868 (e.g. LRP5) and ligands (e.g. WNT6A) are also associated with the migratory
869 phenotypes. Hence LGK974, a Wnt secretion inhibitor, could efficiently abrogate this
870 phenotype. Of note, slightly higher Wnt activity and β -catenin accumulation were also
871 observed in T47D-Y537S cells, but this failed to convert into a migratory phenotype. It is
872 possible that some genes uniquely regulated by Y537S ER in T47D cells might inhibit
873 migratory phenotypes. For instance, the gap junction component, connexin 43, which is
874 exclusively upregulated in T47D-Y537S cells, has been reported to play an inhibitory
875 role in epithelial cell migration (59). Furthermore, the unique observation in T47D rather
876 than MCF7 cell line may be in part explained by the lower basal migratory property and
877 basal Wnt activation in the T47D cell line, which might allow additional gain of function.
878 MCF7 WT cells showed approximately four-fold higher wound closure ratio than T47D
879 at 72 hours (Fig. 5B and Supplementary Fig. S16A) and furthermore it expresses
880 truncated mutant version of LRP5 (60), which confers constitutive Wnt signaling

881 activation. *In vivo* experiments revealed enhanced metastasis in the MCF7-Y537S but
882 not D538G model. This discrepancy with the *in vitro* data could possibly be explained
883 by the longer distant metastatic latency requirement of D538G cells *in vivo*, consistent
884 with a recent study using overexpression cell models (14). Alternatively, it is also
885 plausible that Y537S mutant cells exhibit stronger *in vivo* outgrowth at metastatic sites.
886 Further *in vivo* metastatic experiments in the absence and presence of E2 are
887 warranted to delineate the reason. These data support strong allele and context
888 dependent effects of the *ESR1* mutation on metastatic phenotypes, in line with context
889 dependent effects on transcriptome, cistromes and accessible genome in *ESR1* mutant
890 cells (11,12,14,19). Of note, previous efforts using multiple cell line models with *ESR1*
891 mutations elucidated several congruent molecular and functional alterations associated
892 with endocrine resistance (14,15,54), suggesting that mechanisms underlying
893 metastasis of *ESR1* mutant clones exhibit a higher degree of heterogeneity. This is also
894 supported by clinical data: the recent BOLERO2 trial showed significant differences in
895 overall survival and everolimus response between Y537S and D538G mutations (9),
896 and results from the recent PALOMA3 trial suggest a potential Palbociclib resistance
897 uniquely gained in tumors bearing the Y537S mutation (61). Given our model are limited
898 to MCF7 and T47D cells, there's a pressing need to establish additional *ESR1* mutant
899 models with different background to follow-up on our observation and to perform further
900 pre-clinical investigations. Taken together, these proof-of-concept studies are setting
901 the stage for a more contextual and personalized therapeutic targeting strategy in *ESR1*
902 mutant breast cancer.

903 Of note, our comprehensive clinical investigation from five different cohorts (N=996)
904 suggest that *ESR1* mutations more common in distant compared to local recurrences,
905 which we propose is due to gain-of-function of *ESR1* mutant clones ie those cells are
906 more equipped to escape from the local-regional microenvironment. However, there are
907 some limitations to our study. First, it is challenging to differentiate local recurrences
908 from secondary primary tumors, limiting our analysis. Second, in some of the cohorts
909 we observed significant differences in number of lines of therapy and time to recurrence
910 comparing patients i) with *ESR1* WT vs mutant tumors, and ii) with local and distance
911 recurrences. Although these analyses are limited by different numbers of cases, and

912 data that are available, nevertheless, they suggest that lack of *ESR1* mutation in local
913 recurrences could at least in part be also due to differences in prior therapies as
914 previously reported (6). Of note, a recent study identified hotspot *ESR1* mutations in 15
915 out of 41 (36%) of local-regional ER+ recurrences albeit at significantly lower mutation
916 allele frequencies (62). Given our data presented in this study, together with prior data
917 (14-16), we propose that *ESR1* mutations can facilitate metastatic spread although they
918 might not be sufficient to function as genetic drivers for such events.

919 Lastly, we also sought to address the ER regulatory mechanisms involved in induction
920 of candidate metastatic driver genes utilizing ChIP-seq technology. Interestingly, none
921 of the metastatic candidate genes in *ESR1* mutant cells gained proximal ER binding
922 sites. This could be a result of our stringent hormone deprivation protocol resulting in
923 depletion of weaker binding events, and thus less sensitive binding site readouts. This
924 idea is supported by ChIP-seq data from Harrod et al. (20), which shows stronger ER
925 binding sites around *DSC2*, *DSG2* and *TIMP3* gene loci in MCF7-Y537S cells. Our
926 data, however, clearly shows that ER mutant cells display changes in indirect gene
927 regulation, resulting in metastatic phenotypes. This observation is due to non-canonical
928 ER action on chromatin structure remodeling, which was alternatively validated from our
929 ATAC-seq and FOXA1 ChIP-seq data. We propose that mutant ER reprograms FOXA1,
930 resulting in redistribution of FOXA1 binding to specific enhancers controlling the key
931 migratory driver gene(s). It's also likely that mutant ER can impact FOXA1 occupancy
932 by cooperating with other known epigenetic regulators such as GATA3 (63). In addition,
933 *ESR1* mutations might alter the expression of several important histone modifiers such
934 as KDM5B and KMT2C which showed expression changes in *ESR1* mutant cells.
935 Alteration of histone writers or erasers may reshape global H3K4 methylation and thus
936 differentially recruit FOXA1 (64). These mechanisms warrant future investigation. In
937 addition, several recent studies uncovered the promising role of androgen receptor (AR)
938 in *ESR1* mutant tumors and cell models (18,65), and additional studies are warranted to
939 study de novo interplay between FOXA1, AR and mutant ER.
940 Overall, our study serves as a timely and important preclinical report uncovering
941 mechanistic insights into *ESR1* mutations that can pave the way towards personalized
942 treatment of patients with advanced metastatic breast cancer.

943

944 **Acknowledgement**

945 We are grateful for advice, discussions and technical support from Dr. Ye Qin, Dr. Yu
946 Jiang, Dr. Min Yu, Yonatan Amzaleg and Meghan S. Mooring. We would like to thank
947 Dr. Peilu Wang for her contribution to earlier studies in the Lee-Oesterreich group on
948 *ESR1* mutations. This project used the University of Pittsburgh HSCRF Genomics
949 Research Core, the University of Pittsburgh Center for Research Computing, and the
950 UPMC Hillman Cancer Center Tissue and Research Pathology Services supported in
951 part by NIH grant award P30CA047904. The authors would like to thank the patients
952 who contributed samples to the tissue bank as well as all the clinicians and staff for their
953 efforts in collecting tissues.

954 **Reference**

- 955 1. DeSantis CE, Ma J, Goding Sauer A, Newman LA, Jemal A. Breast cancer statistics, 2017, racial
956 disparity in mortality by state. *CA: a cancer journal for clinicians* **2017**;67:439-48
- 957 2. Turner NC, Neven P, Loibl S, Andre F. Advances in the treatment of advanced oestrogen-
958 receptor-positive breast cancer. *The Lancet* **2017**;389:2403-14
- 959 3. Spoerke JM, Gendreau S, Walter K, Qiu J, Wilson TR, Savage H, *et al.* Heterogeneity and clinical
960 significance of ESR1 mutations in ER-positive metastatic breast cancer patients receiving
961 fulvestrant. *Nature communications* **2016**;7:11579
- 962 4. Robinson DR, Wu Y-M, Vats P, Su F, Lonigro RJ, Cao X, *et al.* Activating ESR1 mutations in
963 hormone-resistant metastatic breast cancer. *Nature genetics* **2013**;45:1446-51
- 964 5. Toy W, Weir H, Razavi P, Lawson M, Goepfert AU, Mazzola AM, *et al.* Activating ESR1 Mutations
965 Differentially Affect the Efficacy of ER Antagonists. *Cancer discovery* **2017**;7:277-87
- 966 6. Schiavon G, Hrebien S, Garcia-Murillas I, Cutts RJ, Pearson A, Tarazona N, *et al.* Analysis of ESR1
967 mutation in circulating tumor DNA demonstrates evolution during therapy for metastatic breast
968 cancer. *Science translational medicine* **2015**;7:313ra182-313ra182
- 969 7. Wang P, Bahreini A, Gyanchandani R, Lucas PC, Hartmaier RJ, Watters RJ, *et al.* Sensitive
970 detection of mono-and polyclonal ESR1 mutations in primary tumors, metastatic lesions, and
971 cell-free DNA of breast cancer patients. *Clinical cancer research* **2016**;22:1130-7
- 972 8. Zhang K, Hong R, Xu F, Xia W, Kaping L, Qin G, *et al.* Clinical value of circulating ESR1 mutations
973 for patients with metastatic breast cancer: a meta-analysis. *Cancer management and research*
974 **2018**;10:2573
- 975 9. Chandralapaty S, Chen D, He W, Sung P, Samoila A, You D, *et al.* Prevalence of ESR1 mutations in
976 cell-free DNA and outcomes in metastatic breast cancer: a secondary analysis of the BOLERO-2
977 clinical trial. *JAMA oncology* **2016**;2:1310-5
- 978 10. Toy W, Shen Y, Won H, Green B, Sakr RA, Will M, *et al.* ESR1 ligand-binding domain mutations in
979 hormone-resistant breast cancer. *Nature genetics* **2013**;45:1439-45
- 980 11. Harrod A, Fulton J, Nguyen VT, Periyasamy M, Ramos-Garcia L, Lai C-F, *et al.* Genomic modelling
981 of the ESR1 Y537S mutation for evaluating function and new therapeutic approaches for
982 metastatic breast cancer. *Oncogene* **2017**;36:2286
- 983 12. Bahreini A, Li Z, Wang P, Levine KM, Tasdemir N, Cao L, *et al.* Mutation site and context
984 dependent effects of ESR1 mutation in genome-edited breast cancer cell models. *Breast Cancer*
985 *Research* **2017**;19:60
- 986 13. Fanning SW, Mayne CG, Dharmarajan V, Carlson KE, Martin TA, Novick SJ, *et al.* Estrogen
987 receptor alpha somatic mutations Y537S and D538G confer breast cancer endocrine resistance
988 by stabilizing the activating function-2 binding conformation. *Elife* **2016**;5
- 989 14. Jeselsohn R, Bergholz JS, Pun M, Cornwell M, Liu W, Nardone A, *et al.* Allele-specific chromatin
990 recruitment and therapeutic vulnerabilities of ESR1 activating mutations. *Cancer cell*
991 **2018**;33:173-86. e5
- 992 15. Yu L, Wang L, Mao C, Duraki D, Kim JE, Huang R, *et al.* Estrogen-Independent Myc
993 Overexpression Confers Endocrine Therapy Resistance on Breast Cancer Cells Expressing
994 ER α Y537S and ER α D538G Mutations. *Cancer letters* **2018**
- 995 16. Merenbakh-Lamin K, Ben-Baruch N, Yeheskel A, Dvir A, Soussan-Gutman L, Jeselsohn R, *et al.*
996 D538G mutation in estrogen receptor- α : A novel mechanism for acquired endocrine resistance
997 in breast cancer. *Cancer research* **2013**;73:6856-64
- 998 17. Gelsomino L, Gu G, Rechoum Y, Beyer AR, Pejerrey SM, Tsimelzon A, *et al.* ESR1 mutations affect
999 anti-proliferative responses to tamoxifen through enhanced cross-talk with IGF signaling. *Breast*
1000 *cancer research and treatment* **2016**;157:253-65

- 1001 18. Gu G, Tian L, Herzog SK, Rechoum Y, Gelsomino L, Gao M, *et al.* Hormonal modulation of ESR1
1002 mutant metastasis. *Oncogene* **2020**:1-15
- 1003 19. Arnesen S, Blanchard Z, Williams MM, Berrett KC, Li Z, Oesterreich S, *et al.* Estrogen receptor
1004 alpha mutations in breast cancer cells cause gene expression changes through constant activity
1005 and secondary effects. *Cancer Research* **2020**:canres.1171.2020
- 1006 20. Harrod A, Fulton J, Nguyen VT, Periyasamy M, Ramos-Garcia L, Lai C-F, *et al.* Genomic modelling
1007 of the ESR1 Y537S mutation for evaluating function and new therapeutic approaches for
1008 metastatic breast cancer. *Oncogene* **2016**
- 1009 21. Tselepis C, Chidgey M, North A, Garrod D. Desmosomal adhesion inhibits invasive behavior.
1010 *Proceedings of the National Academy of Sciences* **1998**;95:8064-9
- 1011 22. Runswick SK, O'Hare MJ, Jones L, Streuli CH, Garrod DR. Desmosomal adhesion regulates
1012 epithelial morphogenesis and cell positioning. *Nature cell biology* **2001**;3:823-30
- 1013 23. Sikora MJ, Cooper KL, Bahreini A, Luthra S, Wang G, Chandran UR, *et al.* Invasive lobular
1014 carcinoma cell lines are characterized by unique estrogen-mediated gene expression patterns
1015 and altered tamoxifen response. *Cancer research* **2014**:canres. 2779.013
- 1016 24. Ianevski A, He L, Aittokallio T, Tang J. SynergyFinder: a web application for analyzing drug
1017 combination dose–response matrix data. *Bioinformatics* **2017**;33:2413-5
- 1018 25. Razavi P, Chang MT, Xu G, Bandlamudi C, Ross DS, Vasan N, *et al.* The Genomic Landscape of
1019 Endocrine-Resistant Advanced Breast Cancers. *Cancer cell* **2018**;34:427-38. e6
- 1020 26. Paul MR, Pan T-c, Pant DK, Shih NN, Chen Y, Harvey KL, *et al.* Genomic landscape of metastatic
1021 breast cancer identifies preferentially dysregulated pathways and targets. *The Journal of Clinical*
1022 *Investigation* **2020**;130
- 1023 27. Pleasance E, Titmuss E, Williamson L, Kwan H, Culibrk L, Zhao EY, *et al.* Pan-cancer analysis of
1024 advanced patient tumors reveals interactions between therapy and genomic landscapes. *Nature*
1025 *Cancer* **2020**;1:452-68
- 1026 28. Fumagalli C, Ranghiero A, Gandini S, Corso F, Taormina S, De Camilli E, *et al.* Inter-tumor
1027 genomic heterogeneity of breast cancers: comprehensive genomic profile of primary early
1028 breast cancers and relapses. *Breast Cancer Research* **2020**;22:1-11
- 1029 29. Priedigkeit N, Hartmaier RJ, Chen Y, Vareslija D, Basudan A, Watters RJ, *et al.* Intrinsic subtype
1030 switching and acquired ERBB2/HER2 amplifications and mutations in breast cancer brain
1031 metastases. *JAMA oncology* **2017**;3:666-71
- 1032 30. Priedigkeit N, Watters RJ, Lucas PC, Basudan A, Bhargava R, Horne W, *et al.* Exome-capture RNA
1033 sequencing of decade-old breast cancers and matched decalcified bone metastases. *JCI insight*
1034 **2017**;2
- 1035 31. Levine KM, Priedigkeit N, Basudan A, Tasdemir N, Sikora MJ, Sokol ES, *et al.* FGFR4
1036 overexpression and hotspot mutations in metastatic ER+ breast cancer are enriched in the
1037 lobular subtype. *NPJ breast cancer* **2019**;5:1-5
- 1038 32. Robinson DR, Wu Y-M, Lonigro RJ, Vats P, Cobain E, Everett J, *et al.* Integrative clinical genomics
1039 of metastatic cancer. *Nature* **2017**;548:297
- 1040 33. Jia S, Miedel MT, Ngo M, Hennesius R, Chen N, Wang P, *et al.* Clinically Observed Estrogen
1041 Receptor Alpha Mutations within the Ligand-Binding Domain Confer Distinguishable
1042 Phenotypes. *Oncology* **2018**;94:176-89
- 1043 34. Aceto N, Bardia A, Miyamoto DT, Donaldson MC, Wittner BS, Spencer JA, *et al.* Circulating tumor
1044 cell clusters are oligoclonal precursors of breast cancer metastasis. *Cell* **2014**;158:1110-22
- 1045 35. Ungefroren H, Sebens S, Seidl D, Lehnert H, Hass R. Interaction of tumor cells with the
1046 microenvironment. *Cell Communication and Signaling* **2011**;9:18
- 1047 36. Friedl P, Locker J, Sahai E, Segall JE. Classifying collective cancer cell invasion. *Nature cell biology*
1048 **2012**;14:777

- 1049 37. Jimenez MA, Tutuncuoglu E, Barge S, Novelli EM, Sundd P. Quantitative microfluidic
1050 fluorescence microscopy to study vaso-occlusion in sickle cell disease. *haematologica*
1051 **2015**;100:e390-e3
- 1052 38. Ao Z, Shah SH, Machlin LM, Parajuli R, Miller PC, Rawal S, *et al.* Identification of cancer-
1053 associated fibroblasts in circulating blood from patients with metastatic breast cancer. *Cancer*
1054 *research* **2015**;75:4681-7
- 1055 39. Tasdemir N, Bossart EA, Li Z, Zhu L, Sikora MJ, Levine KM, *et al.* Comprehensive phenotypic
1056 characterization of human invasive lobular carcinoma cell lines in 2D and 3D cultures. *Cancer*
1057 *research* **2018**;78:6209-22
- 1058 40. Cunha S, Lin Y-C, Goossen EA, DeVette CI, Albertella MR, Thomson S, *et al.* The RON receptor
1059 tyrosine kinase promotes metastasis by triggering MBD4-dependent DNA methylation
1060 reprogramming. *Cell reports* **2014**;6:141-54
- 1061 41. Gkountela S, Castro-Giner F, Szczerba BM, Vetter M, Landin J, Scherrer R, *et al.* Circulating tumor
1062 cell clustering shapes DNA methylation to enable metastasis seeding. *Cell* **2019**;176:98-112. e14
- 1063 42. Cristofanilli M, Pierga J-Y, Reuben J, Rademaker A, Davis AA, Peeters DJ, *et al.* The clinical use of
1064 circulating tumor cells (CTCs) enumeration for staging of metastatic breast cancer (MBC):
1065 International expert consensus paper. *Critical reviews in oncology/hematology* **2019**;134:39-45
- 1066 43. Yu M, Bardia A, Aceto N, Bersani F, Madden MW, Donaldson MC, *et al.* Ex vivo culture of
1067 circulating breast tumor cells for individualized testing of drug susceptibility. *Science*
1068 **2014**;345:216-20
- 1069 44. Need EF, Selth LA, Harris TJ, Birrell SN, Tilley WD, Buchanan G. Research resource: interplay
1070 between the genomic and transcriptional networks of androgen receptor and estrogen receptor
1071 α in luminal breast cancer cells. *Molecular endocrinology* **2012**;26:1941-52
- 1072 45. Creighton CJ, Cordero KE, Larios JM, Miller RS, Johnson MD, Chinnaiyan AM, *et al.* Genes
1073 regulated by estrogen in breast tumor cells in vitro are similarly regulated in vivo in tumor
1074 xenografts and human breast tumors. *Genome biology* **2006**;7:R28
- 1075 46. Li Z, Wu Y, Bahreini A, Priedigkeit NM, Ding K, Sartorius CA, *et al.* ESR1 mutant breast cancers
1076 show elevated basal cytokeratins and immune activation. *bioRxiv* **2020**
- 1077 47. Oyamada M, Takebe K, Oyamada Y. Regulation of connexin expression by transcription factors
1078 and epigenetic mechanisms. *Biochimica et Biophysica Acta (BBA)-Biomembranes*
1079 **2013**;1828:118-33
- 1080 48. Nigam A, Savage F, Boulos P, Stamp G, Liu D, Pignatelli M. Loss of cell-cell and cell-matrix
1081 adhesion molecules in colorectal cancer. *British journal of cancer* **1993**;68:507
- 1082 49. Rege TA, Hagood JS. Thy-1 as a regulator of cell-cell and cell-matrix interactions in axon
1083 regeneration, apoptosis, adhesion, migration, cancer, and fibrosis. *The FASEB journal*
1084 **2006**;20:1045-54
- 1085 50. Anania M, Sensi M, Radaelli E, Miranda C, Vizioli M, Pagliardini S, *et al.* TIMP3 regulates
1086 migration, invasion and in vivo tumorigenicity of thyroid tumor cells. *Oncogene* **2011**;30:3011-
1087 23
- 1088 51. Su C-W, Chang Y-C, Chien M-H, Hsieh Y-H, Chen M-K, Lin C-W, *et al.* Loss of TIMP3 by promoter
1089 methylation of Sp1 binding site promotes oral cancer metastasis. *Cell death & disease*
1090 **2019**;10:1-17
- 1091 52. Zardavas D, Baselga J, Piccart M. Emerging targeted agents in metastatic breast cancer. *Nature*
1092 *reviews Clinical oncology* **2013**;10:191
- 1093 53. Liu J, Pan S, Hsieh MH, Ng N, Sun F, Wang T, *et al.* Targeting Wnt-driven cancer through the
1094 inhibition of Porcupine by LGK974. *Proceedings of the National Academy of Sciences*
1095 **2013**;110:20224-9

- 1096 54. Li Z, Levine KM, Bahreini A, Wang P, Chu D, Park BH, *et al.* Upregulation of IRS1 enhances IGF1
1097 response in Y537S and D538G ESR1 mutant breast cancer cells. *Endocrinology* **2017**;159:285-96
1098 55. Davis AA, Zhang Q, Gerratana L, Shah AN, Zhan Y, Qiang W, *et al.* Association of a novel
1099 circulating tumor DNA next-generating sequencing platform with circulating tumor cells (CTCs)
1100 and CTC clusters in metastatic breast cancer. *Breast Cancer Research* **2019**;21:1-8
1101 56. Gerratana L, Davis AA, Polano M, Zhang Q, Shah AN, Lin C, *et al.* Understanding the organ
1102 tropism of metastatic breast cancer through the combination of liquid biopsy tools. *European*
1103 *Journal of Cancer* **2021**;143:147-57
1104 57. Aasen T, Mesnil M, Naus CC, Lampe PD, Laird DW. Gap junctions and cancer: communicating for
1105 50 years. *Nature Reviews Cancer* **2016**;16:775
1106 58. Xu X, Wang J, Han K, Li S, Xu F, Yang Y. Antimalarial drug mefloquine inhibits nuclear factor
1107 kappa B signaling and induces apoptosis in colorectal cancer cells. *Cancer science*
1108 **2018**;109:1220-9
1109 59. Simpson KJ, Selfors LM, Bui J, Reynolds A, Leake D, Khvorova A, *et al.* Identification of genes that
1110 regulate epithelial cell migration using an siRNA screening approach. *Nature cell biology*
1111 **2008**;10:1027
1112 60. Björklund P, Svedlund J, Olsson A-K, Åkerström G, Westin G. The internally truncated LRP5
1113 receptor presents a therapeutic target in breast cancer. *PloS one* **2009**;4:e4243
1114 61. O'Leary B, Cutts RJ, Liu Y, Hrebien S, Huang X, Fenwick K, *et al.* The genetic landscape and clonal
1115 evolution of breast cancer resistance to palbociclib plus fulvestrant in the PALOMA-3 trial.
1116 *Cancer discovery* **2018**;8:1390-403
1117 62. Zundeleovich A, Dadiani M, Kahana-Edwin S, Itay A, Sella T, Gadot M, *et al.* ESR1 mutations are
1118 frequent in newly diagnosed metastatic and loco-regional recurrence of endocrine-treated
1119 breast cancer and carry worse prognosis. *Breast Cancer Research* **2020**;22:1-11
1120 63. Theodorou V, Stark R, Menon S, Carroll JS. GATA3 acts upstream of FOXA1 in mediating ESR1
1121 binding by shaping enhancer accessibility. *Genome research* **2013**;23:12-22
1122 64. Xhabija B, Kidder BL. KDM5B is a master regulator of the H3K4-methylome in stem cells,
1123 development and cancer. 2019. Elsevier. p 79-85.
1124 65. Williams MM, Spoelstra NS, Arnesen S, O'Neill KI, Christenson JL, Reese J, *et al.* Steroid hormone
1125 receptor and infiltrating immune cell status reveals therapeutic vulnerabilities of ESR1 mutant
1126 breast cancer. *Cancer Research* **2020**

1127

1128

1129

1130 **Table1**

Cohorts	Site of Recurrence	Total Number	<i>ESR1</i> WT	<i>ESR1</i> Mutant	Fisher's Exact p
METAMORPH/POG570/ MSKCC/IEO Merged	Distant	877	722 (82%)	155 (18%)	0.0006
	Local	44	44 (100%)	0 (0%)	
WCRC/Charite	Distant	48	36 (75%)	12 (25%)	0.0031
	Local	27	27 (100%)	0 (0%)	

1131

1132 **Table Legend**

1133 **Table 1. Significant enrichment of *ESR1* mutations in distant compared to local**
1134 **recurrences.**

1135 Upper panel: Data from 877 distant metastatic and 44 local recurrence cases were
1136 merged from three cohorts (METAMORPH, 39 distant/9 local; POG570, 86 distant/14
1137 local; MSKCC, 716 distant/8 local; IEO, 36 distant/13 local). *ESR1* mutation status was
1138 previously identified by whole exome sequencing (METAMORPH), whole genome
1139 sequencing (POG570) or target panel DNA sequencing (MSKCC, IEO). Lower panel: 48
1140 distant ER positive metastases and 27 local ER positive recurrences were obtained
1141 from the WCRC and Charite cohorts. Genomic DNA (gDNA) was isolated from either
1142 FFPE or frozen tumor tissues, and subjected to droplet digital PCR (ddPCR) detection
1143 with specific probes against Y537S, Y537C, Y537N and D538G hotspot point mutations
1144 (cDNA rather than gDNA was used for 3 of the local recurrent samples). Hotspot *ESR1*
1145 mutation incidences between distant metastatic and local recurrent samples in both
1146 panels were compared using a Fisher's exact test.

1147

1148 **Figure legends**

1149

1150 **Figure 1. Transcriptomic landscape of *ESR1* mutant metastatic breast cancers.**

1151 A. Schematic overview of transcriptomic analysis of four ER+ metastatic breast cancer
1152 cohorts.

1153 B. Box plots representing the enrichment levels of “Estrogen Response Early” and
1154 “Estrogen Response Late” signatures in *ESR1* mutant versus *ESR1* WT metastatic
1155 tumors in each cohort. (WCRC, 46 *ESR1* WT/8 mutant; MET500, 34 *ESR1* WT/12
1156 *ESR1* mutant; DFCI, 98 *ESR1* WT/32 mutant; POG570, 68 *ESR1* WT/18 mutant). Four
1157 quantiles are shown in each plot. Mann-Whitney U test was used to compare the
1158 enrichment of the signatures in WT and mutant tumors. (* $p < 0.05$, ** $p < 0.01$)

1159 C. Volcano plots representing the differentially expressing genes (DE genes) in *ESR1*
1160 mutant tumors versus WT tumors in the three metastatic breast cancer cohorts. DE
1161 genes were selected using the cutoff of $FDR < 0.1$ and $|\log_2FC| > 1.5$. Genes that were
1162 upregulated or downregulated were labelled in red and blue respectively with
1163 corresponding counts.

1164 D. Dot plots showing the top 5 altered cellular and molecular functional categories
1165 derived from DE genes analysis using Ingenuity Pathway Analysis software. Specific
1166 sub-functions within overarching categories are presented as individual dots.
1167 Consistently altered pathways across all four cohorts are indicated in red.

1168 E. Stacked bar plot showing the distribution of 14 hotspot *ESR1* mutations identified in
1169 six independent cohorts using unbiased DNA sequencing approaches. Specific sample
1170 numbers were indicated in the plots. Variants with percentages above 1% were labelled
1171 on the top of each bar.

1172 F. Scatterplot representing enrichment level distribution of 50 hallmark gene sets in 10
1173 Y537S and 8 D538G metastatic tumors (after being normalized against 98 WT
1174 counterparts) from the DFCI cohort. Top enriched pathways from each quartile are
1175 labelled.

1176

1177 **Figure 2. *ESR1* mutant cells exhibit stronger cell-cell adhesion.**

1178 A. Representative images of day 6 hormone deprived MCF7 and T47D spheroids
1179 seeded in 6-well ultra-low attachment (ULA) plates. Images were taken under 1.25x
1180 magnification. Representative experiment from three independent repeats is shown.
1181 B. Bar plot representing day 7 cell numbers of MCF7 or T47D WT and *ESR1* mutant
1182 cells seeded into flat bottom ULA plates. Cell abundance were quantified using Celltiter
1183 Glo. Fluorescence readouts were corrected to background measurements. Each bar
1184 represents mean \pm SD with 10 (MCF7) or 6 (T47D) biological replicates. Representative
1185 experiment from six independent repeats is shown. Dunnett's test was used between
1186 WT and each mutant. (** $p < 0.01$)
1187 C. Left panel: A calcein labelled cell-cell adhesion assay was performed in MCF7 WT
1188 and mutant cells. Adhesion ratios were calculated by dividing the remaining cells after
1189 each wash to the initial readout from unwashed wells. A pairwise two-way ANOVA
1190 between WT and each mutant was utilized. Each point represents mean \pm SD with five
1191 biological replicates. Representative experiment from 17 independent repeats is shown.
1192 Right panel: Adhesion ratios after three washes were extracted from 17 independent
1193 experiments displayed as mean \pm SEM. Dunnett's test was used to compare between
1194 WT and each mutant. (* $p < 0.05$, ** $p < 0.01$)
1195 D. Line plot representing the aggregation ratio of MCF7 cells seeded into round bottom
1196 ULA plates. Cell aggregation processes were followed by the IncuCyte living imaging
1197 system every hour. Spheroid areas were normalized to time 0. Each dot represents
1198 mean \pm SD with eight biological replicates. Representative images after 3 hours of
1199 aggregation are shown across the top panel. Images were captured under 10x
1200 magnification. Representative experiment from five independent repeats is shown. A
1201 pairwise two-way ANOVA between WT and each mutant was utilized. (** $p < 0.01$)
1202 E. Representative images of MCF7 cell cluster status after two hours of flow under
1203 physiological shear stress produced by the ibidi microfluidic system. Images were taken
1204 under 10x magnification. A regional 2x zoom in is presented on the top of each image.
1205 Representative experiment from three independent repeats is shown.
1206 F. Bar graph representing the percentage of MCF7 cells in a cluster based on the
1207 quantification of cluster and single cell numbers from 12 representative images per
1208 group. Each bar represents mean \pm SD. Cell cluster ratios after 2 hours of flow were

1209 further normalized to time 0 to correct for baseline pre-existing clusters. Representative
1210 experiment from three independent repeats is shown. Dunnett's test was used between
1211 WT and mutant cells. (** $p < 0.01$)

1212 G. Bar plots showing the cluster size distribution of MCF7 cells after normalization to
1213 time 0. Each bar represents mean \pm SD from 12 representative images per group.
1214 Representative experiment from three independent repeats is shown. Dunnett's test
1215 was used between WT and each mutant cell type within the same cluster size category.
1216 (** $p < 0.01$).

1217 H. Schematic overview of short-term *in vivo* circulating tumor cell evaluation
1218 experimental procedure.

1219 I. Left panel: Representative images of two-cell clusters (WT) and a multicellular cluster
1220 (Y537S). Images were taken under 40x magnification. Right panel: Stacked bar chart
1221 representing the distribution of cancer cells in each cluster type. This experiment was
1222 performed once. Fisher's exact test was applied to test whether multicellular clusters
1223 were enriched in *ESR1* mutant cells. (** $p < 0.01$)

1224 J. Left panel: Representative images of a WT and Y537S two cell cluster. Lines
1225 connecting the two nuclei centers were indicated. Images were taken under 40x
1226 magnification. Right panel: Dot plot represents the inter-nuclei distance of all two-cell
1227 clusters in MCF7 WT and mutant cells. Measured distances were normalized to the
1228 average radius of both cells of this cluster size to avoid cell size bias. This experiment
1229 was performed once. Mann-Whitney U test was performed between WT and each
1230 mutant cell. (** $p < 0.01$)

1231 K. Schematic overview of *in vivo* metastatic evaluation of *ESR1* mutant cells introduced
1232 via tail vein injections.

1233 L. Representative H&E staining images the tumorous portion of MCF7-Y537S induced
1234 macro-metastatic (macro-met) tumors from 3 different mice. This experiment was
1235 performed once. Images were taken under 20x magnification.

1236 M. Left panel: Dot plots showing the number of macro-met per mouse from MCF7 *ESR1*
1237 WT and mutant cells-injected mice. Pairwise Mann-Whitney U test was used to
1238 compare the macro-met numbers in each mutant group to WT cell-injected groups.

1239 Right panel: Quantification of lung micro-met areas based on human specific CK19

1240 staining quantification. This experiment was performed once. Pairwise Mann-Whitney U
1241 test was applied for statistical analysis. (WT, n=7; Y537S, n=6; D538G, n=7) (* p<0.05)
1242 N. Representative images of micro-metastatic loci on the lung sections of T47D-*ESR1*
1243 mutant cell-injected mice. Images were taken under 10x magnification. Metastatic loci
1244 were indicated with white arrow. This experiment was p once. (WT, n=7; Y537S, n=6;
1245 D538G, n=7) (Blue: nuclei; Red: CK8+18; Green: Human specific CK19)
1246 O. Left panel: Dot plots showing the macro-metastatic counts per mouse from T47D
1247 *ESR1* mutant-injected mice. Pairwise Mann-Whitney U test was used to compare the
1248 macro-met numbers in each mutant group to WT cell-injected groups. Right panel:
1249 Quantification of lung micro-met areas based on CK19 staining and was performed in a
1250 blind manner. This experiment was performed once. Pairwise Mann-Whitney U test was
1251 applied for statistical analysis. (N=1, * p<0.05)
1252 P. Representative images of CTCs clusters detected through the CellSearch Platform
1253 after EpCAM dependent enrichment (Pink: nuclei, Green: CK8/CK18/CK 19). Image
1254 resolution and magnification were achieved in accordance with the CellSearch Platform.
1255 Q. Mosaic plot showing the association between *ESR1* genotype status and clustered
1256 CTCs. A significant positive association was observed by Fisher's exact test between
1257 *ESR1* mutations and high clustered CTCs (clustered CTCs > 4).
1258 R. Kaplan Meier plot representing the impact of clustered CTCs in terms of Overall
1259 Survival (OS). Patients with clustered CTCs > 4 experienced the worse prognosis in
1260 terms of OS both with respect to those without clusters (both stage IV indolent and
1261 stage IV aggressive) and those with clusters but with ≤ 4 clustered CTCs (P < 0.0001).
1262 Patients at risk are reported at each time point. Log rank test was to compare the
1263 survival curves of the two patient subsets.

1264

1265 **Figure 3. Desmosome and gap junction adhesome reprogramming confers**
1266 **enhanced adhesive properties in *ESR1* mutant cells.**

1267 A. Gene Set Variation Analysis (GSVA) scores of desmosome and gap junction gene
1268 sets enrichment in MCF7 and T47D *ESR1* mutant vs WT cell RNA-seq data sets. Each
1269 cell type has four biological replicates. Dunnett's test was used to test the significance
1270 between WT and mutant cell lines. (** p<0.01)

1271 B. Heatmaps showing all desmosome and gap junction component genes in MCF7 and
1272 T47D *ESR1* mutant cells. Data were extracted from RNA-sequencing results with four
1273 biological replicates. Color scale represents the Log₂ fold changes in each mutant
1274 normalized to WT counterparts using the log₂(TPM+1) expression matrix. Genes with
1275 counts=0 in more than one replicate in each cell type were filtered out of analysis.
1276 Genes with a log₂FC>1.2 and a p<0.05 in at least one group are labelled in red.

1277 C. Western blot validation of the expression level of *DSG2*, *DSC1*, *PKP1*, Cx43 and
1278 Cx26 in MCF7 WT and *ESR1* mutant cells after hormone deprivation. Tubulin was
1279 blotted as a loading control. Representative blots from three independent repeats was
1280 shown for each protein.

1281 D. qRT-PCR validation of selected altered candidate desmosome and gap junction
1282 genes in MCF7 *ESR1* mutant cells. $\Delta\Delta C_t$ method was used to analyze relative mRNA
1283 fold changes normalized to WT cells and *RPLP0* levels were measured as an internal
1284 control. Each bar represents mean \pm SD with biological triplicates. This experiment was
1285 a representative from four independent repeats. Dunnett's test was used to compare the
1286 gene expression between WT and each mutant. (* p<0.05, ** p<0.01)

1287 E. Representative images of immunofluorescence staining showing the distribution of
1288 desmoglein 2 (*DSG2*) in MCF7 WT and *ESR1* mutant cells. Images were taken under
1289 20x magnification. A 2x zoom in of each image is presented. Right lower panel: *DSG2*
1290 signal intensities were quantified and normalized to cell numbers in each image. Data
1291 from 20 regions within the collected images were combined from four independent
1292 experiments. Mean \pm SD is presented in each plot. Dunnett's test was used to test the
1293 significance between WT and mutant cells. (** p<0.01)

1294 F. Box plots representing GSVA scores of the enrichment of the top desmosome and
1295 gap junction candidate genes (genes with log₂FC>2 in at least one mutant line) in
1296 patient matched primary-metastatic paired samples. Delta GSVA score of each sample
1297 was calculated by subtracting the scores of primary tumors from the matched metastatic
1298 tumors. Four quantiles are shown in each plot. Mann-Whitney U test was performed to
1299 compare the Delta GSVA scores between *ESR1* WT (n=44) and mutation (n=7)
1300 harboring tumors. (* p<0.05)

1301 G & J. Representative images of cell cluster status after two hours of flow under
1302 physiological shear stress in the ibidi microfluidic system, with or without 300 μ M of the
1303 desmosomal blocking peptide (G) or 100 μ M of carbenoxolone (J) treatment. Images
1304 were taken under 10x magnification. This experiment was a representative from two
1305 (desmosome peptide treatment) and three (CBX treatment) independent repeats.
1306 H & K. Bar graphs representing the T0 normalized percentage of cells in cluster status
1307 after quantification of cluster and single cell numbers under each treatment. Each bar
1308 represents mean \pm SD quantified from 12 images per group. This experiment was a
1309 representative from two (desmosome peptide treatment) and three (CBX treatment)
1310 independent repeats. Student's t test was used to examine the effects of treatment
1311 between each group's cluster ratio. (** $p < 0.01$)
1312 I & L. Bar graphs representing the T0 normalized 2 cell and greater than 5 cell cluster
1313 percentages under each treatment. Each bar represents mean \pm SD quantified from 12
1314 images per group. This experiment was a representative from two (desmosome peptide
1315 treatment) and three (CBX treatment) independent repeats. Pairwise student's t test
1316 was used to examine the effects of treatment between each group's cluster ratio. (**
1317 $p < 0.01$)
1318 M. Bar graphs representing qRT-PCR measurement of *DSC1*, *DSC2*, *GJA1*, *GJB2* and
1319 *GJB5* mRNA levels in MCF7 WT and *ESR1* mutant cells following siRNA knockdown of
1320 *ESR1* for 7 days. $\Delta\Delta$ Ct method was used to analyze relative mRNA fold changes
1321 normalized to WT cells and *RPLP0* levels were measured as an internal control. Each
1322 bar represents mean \pm SD with three biological replicates. Representative experiment
1323 from three independent repeats is displayed. Student's t test was used to compare the
1324 gene expression between scramble and knockdown groups of each cell type. (* $p < 0.05$,
1325 ** $p < 0.01$)
1326 N & O. Western blot validation of the expression level of ER, Cx43 and cFOS in MCF7
1327 WT and *ESR1* mutant cells after seven days of *ESR1* knockdown (N) or three days of
1328 20 μ M T-5224 treatment (O). Tubulin was blotted as a loading control. Representative
1329 blot from three (N) and five (O) independent repeats is displayed.
1330 P. Screen shot of H3K27ac and H3K4me2 binding peaks at proximity to genomic *DSC1*
1331 and *DSG1* loci in MCF7 parental cells. ChIP-seq data were visualized at WashU

1332 Genome Browser based on public available data set from ENCODE (H3K4me2:
1333 ENCSR875KOJ ; H3K27ac: ENCSR752UOD). Y axis represents the binding intensity of
1334 each ChIP-seq data set. Selected peaks for ChIP-qPCR assessment in Q were
1335 indicated.

1336 Q. Bar graph showing the fold enrichment levels of the two active histone modification
1337 markers at the two selected peaks around *DSC1* and *DSG1* gene loci illustrated in P.
1338 Each bar represents mean \pm SD from biological triplicates. Fold enrichment levels were
1339 calculated by normalizing to IgG controls and further normalized to WT levels. This
1340 experiment is representative from two independent repeats. Dunnett's test was used
1341 within each group. (N=2, * $p<0.05$, ** $p<0.01$)

1342

1343 **Figure 4. *ESR1* mutant cells show diminished ECM adhesion and enhanced**
1344 **invasion via an altered *TIMP3*-MMP axis.**

1345 A. Gene set enrichment plots showing the comparison of enrichment levels of the
1346 "KEGG ECM Receptor Interaction" gene set (MSigDB, M7098) between WT and mutant
1347 tumors in DFCI cohort. (98 *ESR1* WT and 32 mutant tumors)

1348 B. Heatmap representation of adhesion ratio on 7 ECM components performed with
1349 MCF7 and T47D *ESR1* WT and mutant cells. Adhesion ratio of each condition with
1350 biological quadruplicates was quantified by dividing the number of remaining cells after
1351 washing to the original total cells plated. All data was further normalized to WT cells
1352 within each cell line. This experiment was performed once. Dunnett's test was applied to
1353 each condition of each cell line. (* $p<0.05$, ** $p<0.01$)

1354 C. Representative images *ESR1* WT and mutant cells remaining on collagen I after
1355 three PBS washes. Images were taken using 4x magnification. Experiment displayed is
1356 representative from three independent repeats.

1357 D. Quantification of adhesion ratios on collagen I in each cell type. Bar graphs represent
1358 the mean \pm SD with four biological replicates in each group. Dunnett's test was utilized
1359 within each cell line to compare WT and mutant adhesion ratios. Experiment displayed
1360 is representative from 12 (MCF7) and 11 (T47D) independent repeats. (* $p<0.05$, **
1361 $p<0.01$)

1362 E. Volcano plots showing the alterations of 84 ECM adhesion genes in all mutant cell
1363 types in a pairwise comparison to the WT counterparts. Genes were pre-filtered with an
1364 average Ct<35 in at least one group. An FDR<0.1 was considered as a significantly
1365 altered gene in *ESR1* mutant cells. Overlapping downregulated (blue) or upregulated
1366 (red) genes between the two mutants of each cell line were further highlighted, with
1367 gene name labels for the top targets. Top changed genes in each T47D mutant cells
1368 were labelled in green. This experiment was performed once.

1369 F. Venn diagrams showing the consistently differentially expressed genes between the
1370 two mutant variants within each cell line. *TIMP3* was highlighted as the only overlapping
1371 gene in all four *ESR1* mutant cell types.

1372 G. qRT-PCR validation of *TIMP3* expression in WT and *ESR1* mutant cells. Ct values
1373 were normalized to *RPLP0* and further normalized to WT cells. Bar graphs represent
1374 the mean \pm SD with biological triplicates in each group. Representative experiment from
1375 seven independent repeats is shown. Dunnett's test was utilized within each cell line. (*
1376 $p<0.05$, ** $p<0.01$)

1377 H. Western blot validation of *TIMP3* from whole cell lysates after hormone deprivation.
1378 Tubulin was used as a loading control. Representative experiment from six independent
1379 repeats is shown.

1380 I & J. Quantification of adhesion ratios on collagen I in each mutant variant following
1381 transfection of pcDNA empty vector or *TIMP3* plasmids in MCF7 (I) and T47D (J) cell
1382 models. Bar graphs represent the mean \pm SD from 5 (MCF7) and 7 (T47D) biological
1383 replicates. Representative experiment from four independent repeats is shown.

1384 Student's t test was used to compare the empty vector and *TIMP3* overexpressing
1385 groups. (* $p<0.05$, ** $p<0.01$)

1386 K & L. Graphical view of pan-MMP FRET kinetic assay. MMPs in MCF7 (K) and T47D
1387 (L) cell lysates were pre-activated and mixed with MMP substrates. Fluorescence was
1388 measured in a time course manner and normalized to T0 baseline and further
1389 normalized to WT cell readouts. Each point represents the mean \pm SD value from three
1390 biological replicates. Representative experiment from four independent repeats is
1391 shown. Pairwise two-way ANOVA between WT and each mutant cell type was
1392 performed. (* $p<0.05$, ** $p<0.01$)

1393 M. Top panel: Representative images of the spheroid-based collagen invasion assay in
1394 *ESR1* WT and mutant cell models. MCF7 and T47D spheroids were mixed in collagen I
1395 for 4 and 6 days, respectively. Bright field images were taken accordingly with 10x
1396 magnification. Bottom panel: Quantification of invasive areas within images. Invasive
1397 areas were calculated by subtracting each original spheroid area from the
1398 corresponding endpoint total area. Each bar represents mean \pm SD with 10 biological
1399 replicates. Experiments displayed are representative from three independent repeats
1400 from each cell line. Dunnett's test was used to compare the difference between WT and
1401 mutant cells. (* $p < 0.05$, ** $p < 0.01$)

1402 N. Representative images of the spheroid-based collagen invasion assay with 10 μ M of
1403 Marimastat treatment in MCF7 (Top panel) and T47D (Lower panel) cell models for 4
1404 and 6 days, respectively. Images were taken under 10x magnification. Experiment was
1405 performed with 20 biological replicates for once.

1406 O. Quantification of corresponding invasive areas from N. Student's t test was used to
1407 compare the effects of Marimastat treatment to vehicle control. (** $p < 0.01$)

1408

1409 **Figure 5. *De novo* FOXA1-mediated Wnt pathway activation enhances migratory**
1410 **property of the T47D-D538G cells.**

1411 A & B. Representative images (A) and quantification (B) of wound scratch assay of
1412 T47D WT and *ESR1* mutant cells performed using IncuCyte living imaging system over
1413 72 hours. The migratory region normalized to T0 are labelled in blue. Images were
1414 taken under 10x magnification. Cell migration rates were quantified based on relative
1415 wound densities with 8 biological replicates. Representative experiment from 11
1416 independent repeats is shown. Pairwise two-way ANOVA between WT and each mutant
1417 was performed. (** $p < 0.01$)

1418 C. Representative magnified images of the migratory edge of each group in wound
1419 scratch assays in A.

1420 D & E. Representative images (D) and quantification (E) of spheroid collective migration
1421 assays in T47D mutant cells. T47D cells were initially seeded into round bottom ULA
1422 plates to form spheroids, which were then transferred onto collagen I coated plates.

1423 Collective migration was measured after 4 days. The migratory edge of each spheroid is

1424 circled with a white line. Migratory distances were calculated based on the mean radius
1425 of each spheroid normalized to corresponding original areas. Representative
1426 experiment from three independent repeats is shown. Dunnett's test was used for
1427 statistical analysis. (** $p < 0.01$)

1428 F. Dot plots representing the enrichment distribution of the 50 MSigDB curated Hallmark
1429 gene sets in T47D-Y537S and T47D-D538G models normalized to WT cells.
1430 Significantly enriched gene sets ($FDR < 0.25$) are highlighted in red, with names labeled
1431 in the venn diagram plot on the right panel. Gene sets enriched in Y537S and D538G
1432 cell models are in green and blue circles respectively.

1433 G. Immunoblot detection of β -catenin, phospho-GSK3 β (Ser9), phospho-GSK3 α
1434 (Ser21) total GSK3 β and total GSK3 α levels in T47D WT and mutant cells after
1435 hormone deprivation. Tubulin was blotted as a loading control. Representative blots
1436 from three independent repeats is displayed for each protein.

1437 H. Quantification of IncuCyte wound scratch assay with or without 5 μ M LGK974
1438 treatment for 72 hours. The migratory region normalized to T0 are labelled in blue.
1439 Images were taken under 10x magnification. Cell migration rates were quantified based
1440 on relative wound densities with eight biological replicates. Representative experiment
1441 from three independent repeats is shown. Pairwise two-way ANOVA between WT and
1442 each mutant was performed. (** $p < 0.01$)

1443 I. IncuCyte migration assay with combination treatment of four different doses of
1444 LGK974 and Fulvestrant in T47D-D538G cells. Inhibition rates were calculated using
1445 the wound density at 48 hours normalized to vehicle control with values labelled using
1446 color scales in the heatmap. Positive Bliss scores are considered a synergistic
1447 combination. Representative experiment from three independent repeats is shown.

1448 J. Dot plot representing the fold changes of all Wnt signaling component genes in both
1449 T47D *ESR1* mutant cell models normalized to WT cells. The blue dotted frame
1450 highlights the unique T47D-D538G enriched genes as well as genes that are enriched
1451 in both mutants, but with a larger magnitude of enrichment in the T47D-D538G cells.

1452 K & L. Immunoblot validation of Fulvestrant-induced ER degradation (K) and FOXA1
1453 knockdown (L). Cell lysates were subjected to ER and FOXA1 detection. Tubulin was
1454 blotted as a loading control. These validation experiments were performed once.

1455 M & N. Wound scratch assay in T47D-D538G and WT cells with 1 μ M of Fulvestrant
1456 treatment (M) or knockdown of FOXA1 (N) for 72 hours. Cell migration rates were
1457 quantified based on wound closure density. For fulvestrant treatment, data were merged
1458 from 3 (WT) or 6 (D538G) independent experiments. For FOXA1 knockdown,
1459 representative result from three independent repeats is displayed. Pairwise two-way
1460 ANOVA between siScramble/siFOXA1 or vehicle/Fulvestrant conditions in each cell
1461 type was performed. (* $p < 0.05$, ** $p < 0.01$)

1462 O. PCA plot showing the FOXA1 peak distribution of T47D WT, WT+E2, T47D-Y537S
1463 and T47D-D538G groups.

1464 P. Heatmaps representing the comparison of FOXA1 binding intensities in T47D-D538G
1465 mutants to FOXA1 binding in WT cells. Displayed in a horizontal window of ± 2 kb from
1466 the peak center. The pairwise comparison between WT and mutant samples was
1467 performed to calculate the fold change (FC) of intensities. Binding sites were sub-
1468 classified into sites with increased intensity ($FC > 2$), decreased intensity ($FC < -2$), and
1469 non-changed intensity ($-2 < FC < 2$). Percentages of each subgroup are labelled on the
1470 heatmaps.

1471 Q. Bar charts showing the percentage of ATAC peaks overlapping (black) or not
1472 overlapping (grey) with FOXA1 binding sites in T47D-WT, T47D-Y537S and T47D-
1473 D538G cells.

1474 R. Venn diagram showing the intersection of genes annotated from dually gained ATAC
1475 and FOXA1 peaks (± 3 kb of TSS with 200kb of the peak flank) and RNA-seq
1476 differentially expressed non-canonical ligand-independent genes (gene with $|\text{fold}$
1477 $\text{change}| > 2$, $\text{FDR} < 0.005$ in D538G vs WT excluding genes with $|\text{fold change}| > 1.5$,
1478 $\text{FDR} < 0.01$ in WT+E2 vs WT groups). *TCF4* is highlighted.

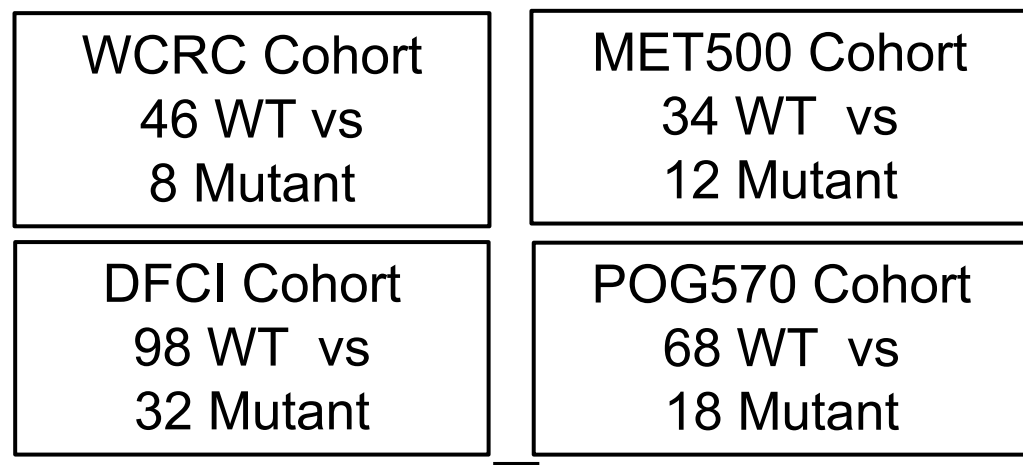
1479 S. Wound scratch assay in T47D-WT and T47D-D538G cells with or without prior
1480 transfection of a dominant negative *TCF4* plasmid for 72 hours. Pairwise two-way
1481 ANOVA between vehicle and treatment conditions was performed. Data from one
1482 representative experiment of three independent experiments (each with six biological
1483 repeats) is shown. (** $p < 0.01$)

1484

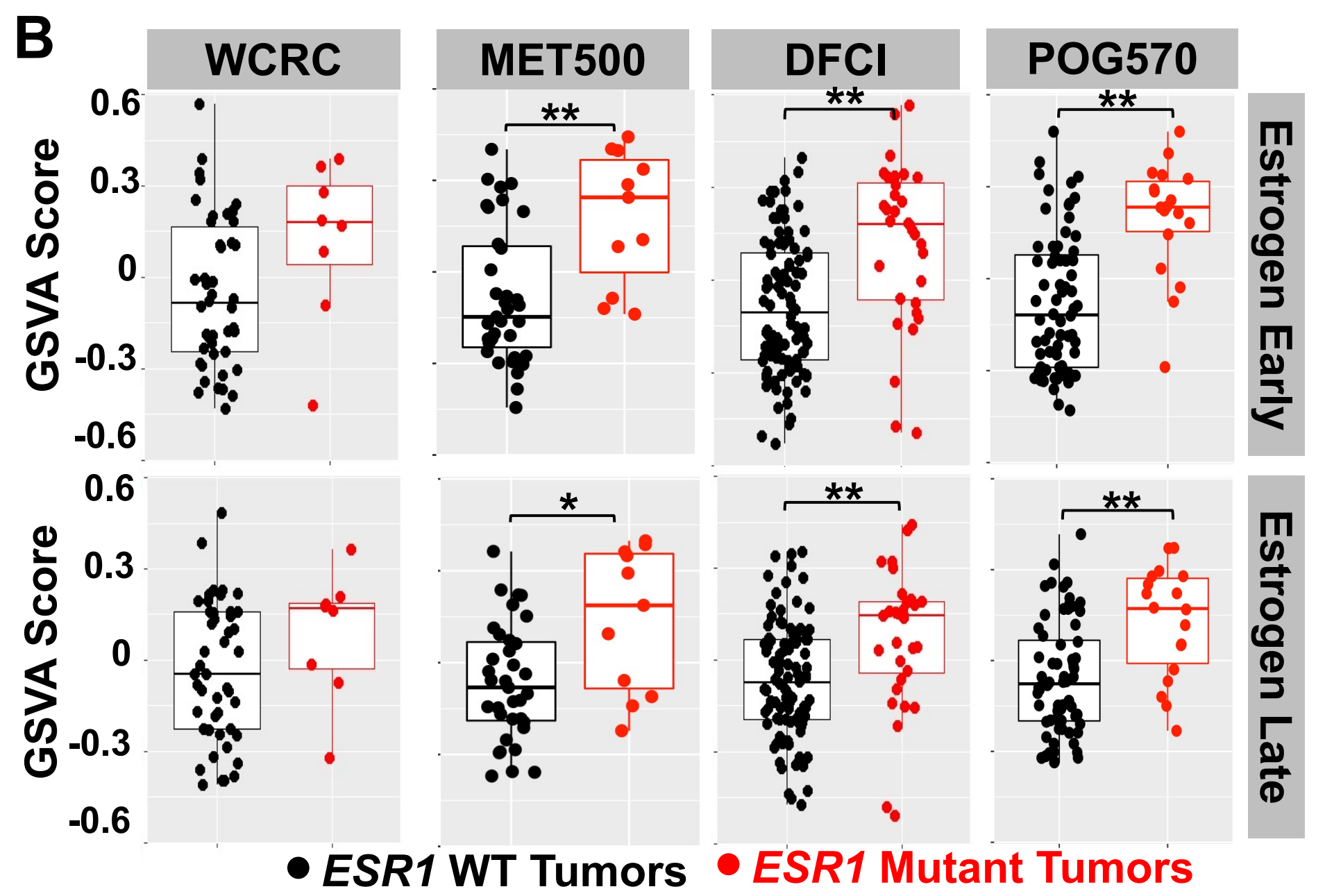
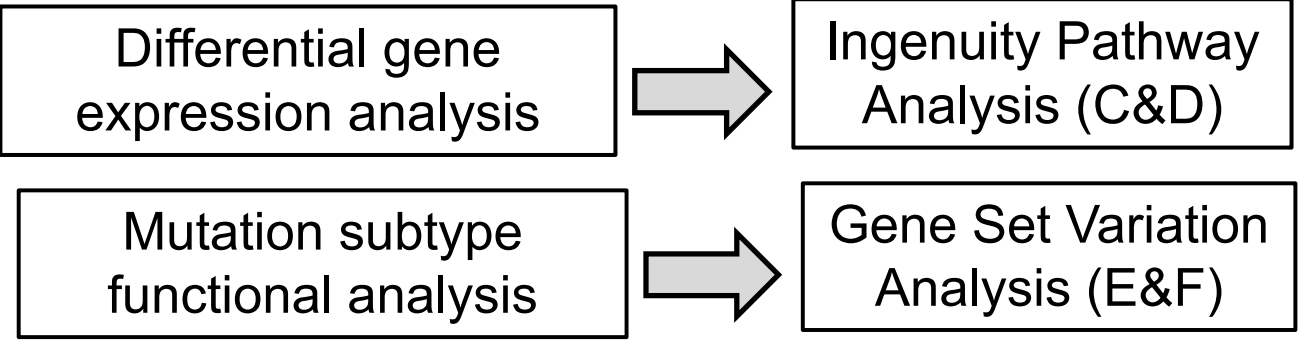
1485

Figure 1

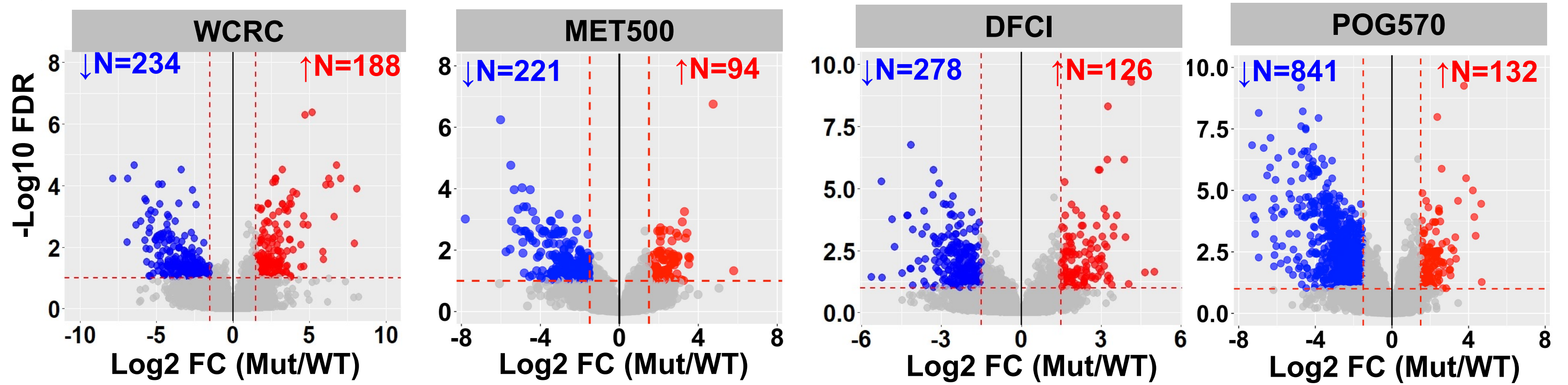
A ER+ Metastatic Tumor Cohorts



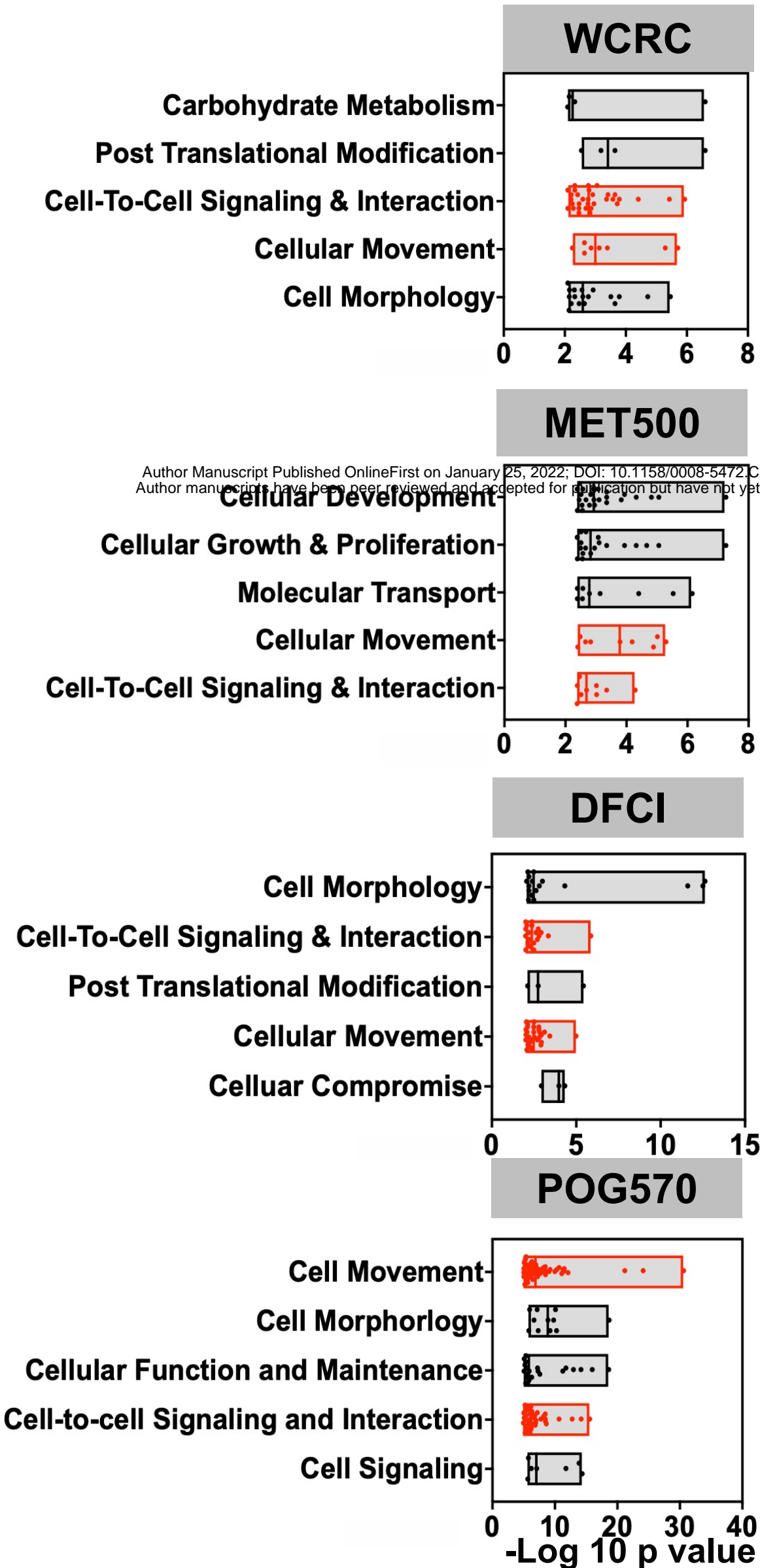
Gene Set Enrichment Analysis QC
Estrogen Response Early/Late Signatures (B)



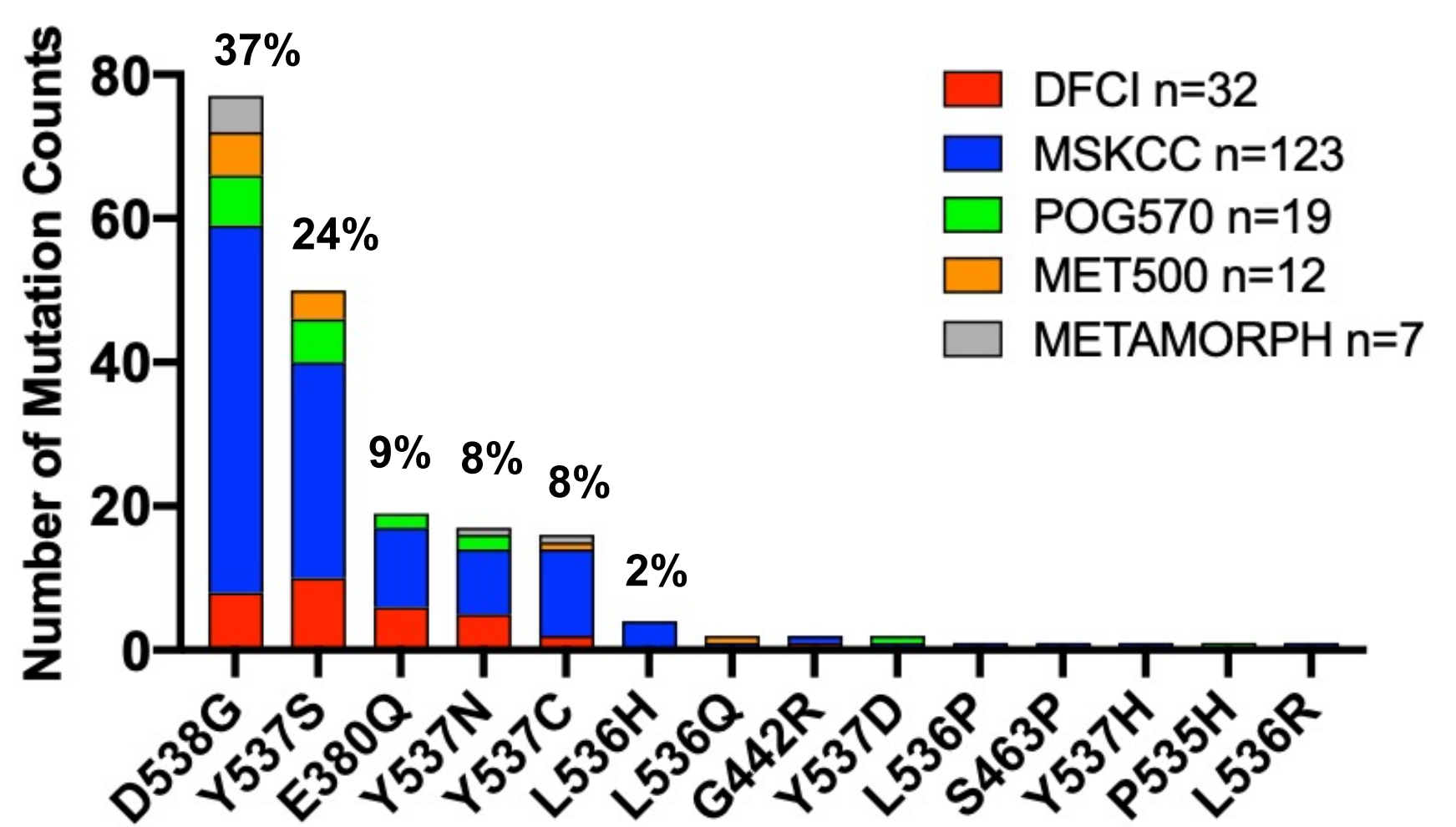
C Differentially Expressed Genes



D Top 5 Altered Molecular & Cellular Functions



E Mutant Variants Distribution



F Mutation Variants-Specific Hallmark Gene Set Enrichment Alteration

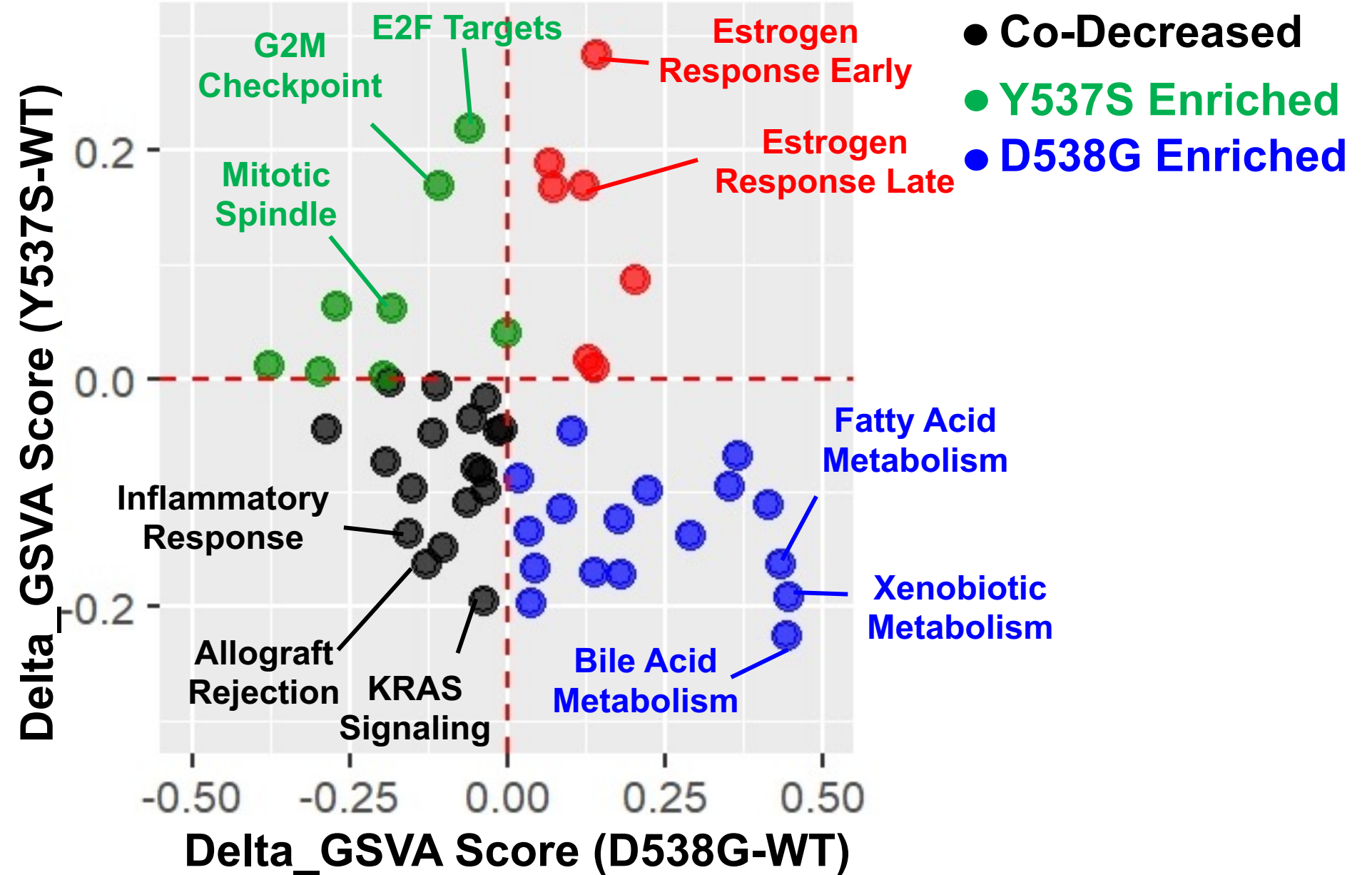


Figure 2

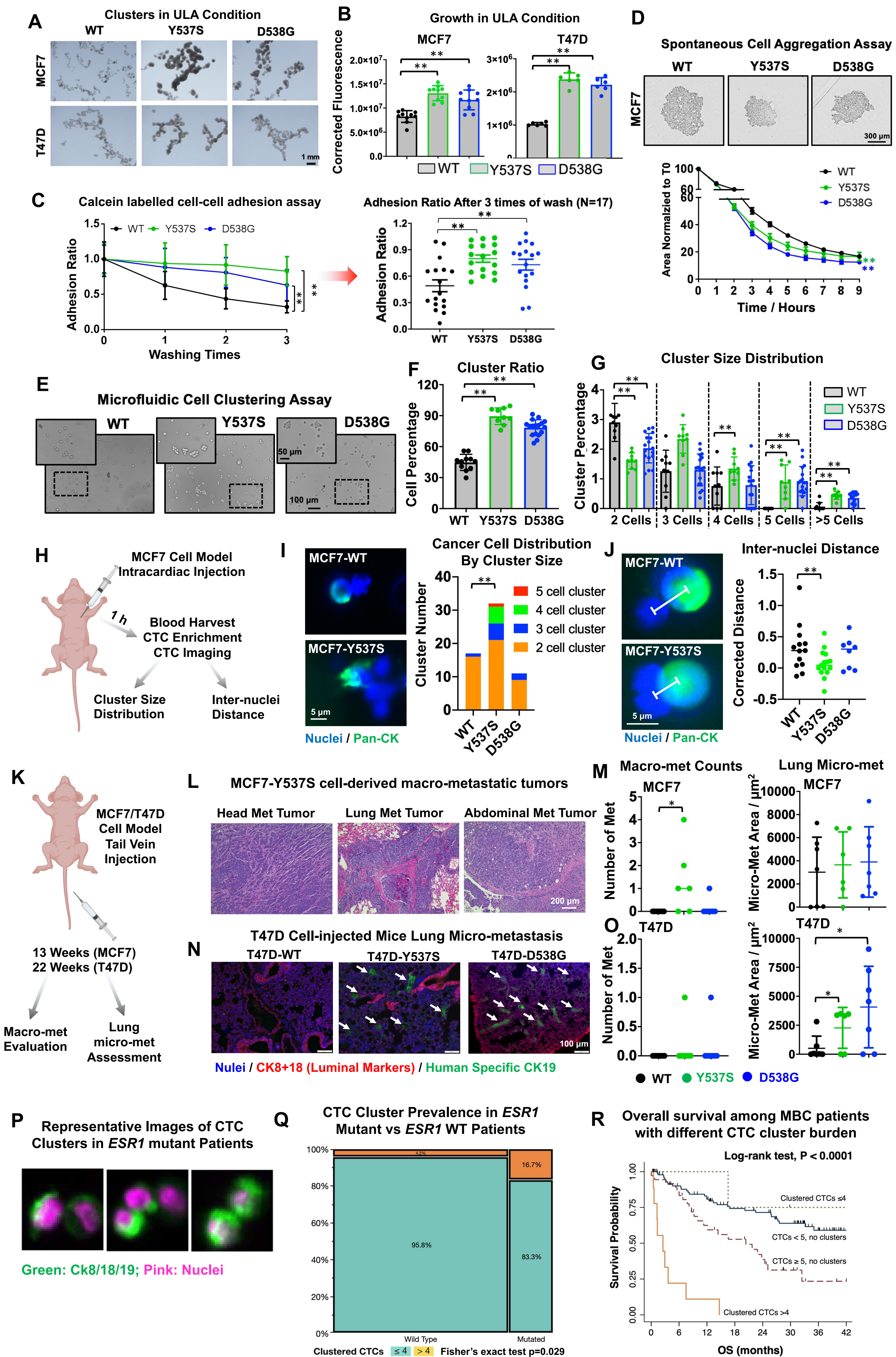


Figure 3

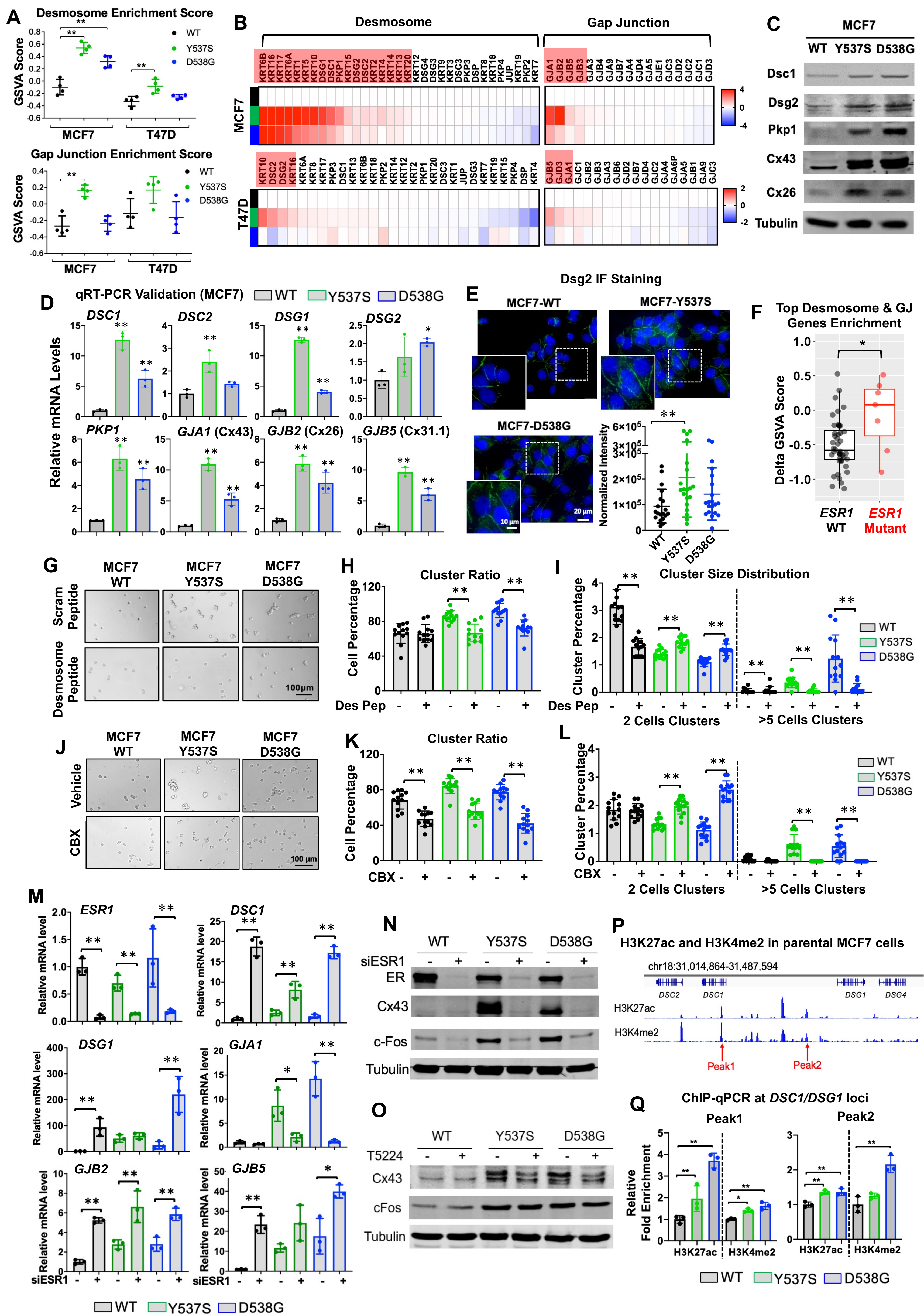


Figure 4

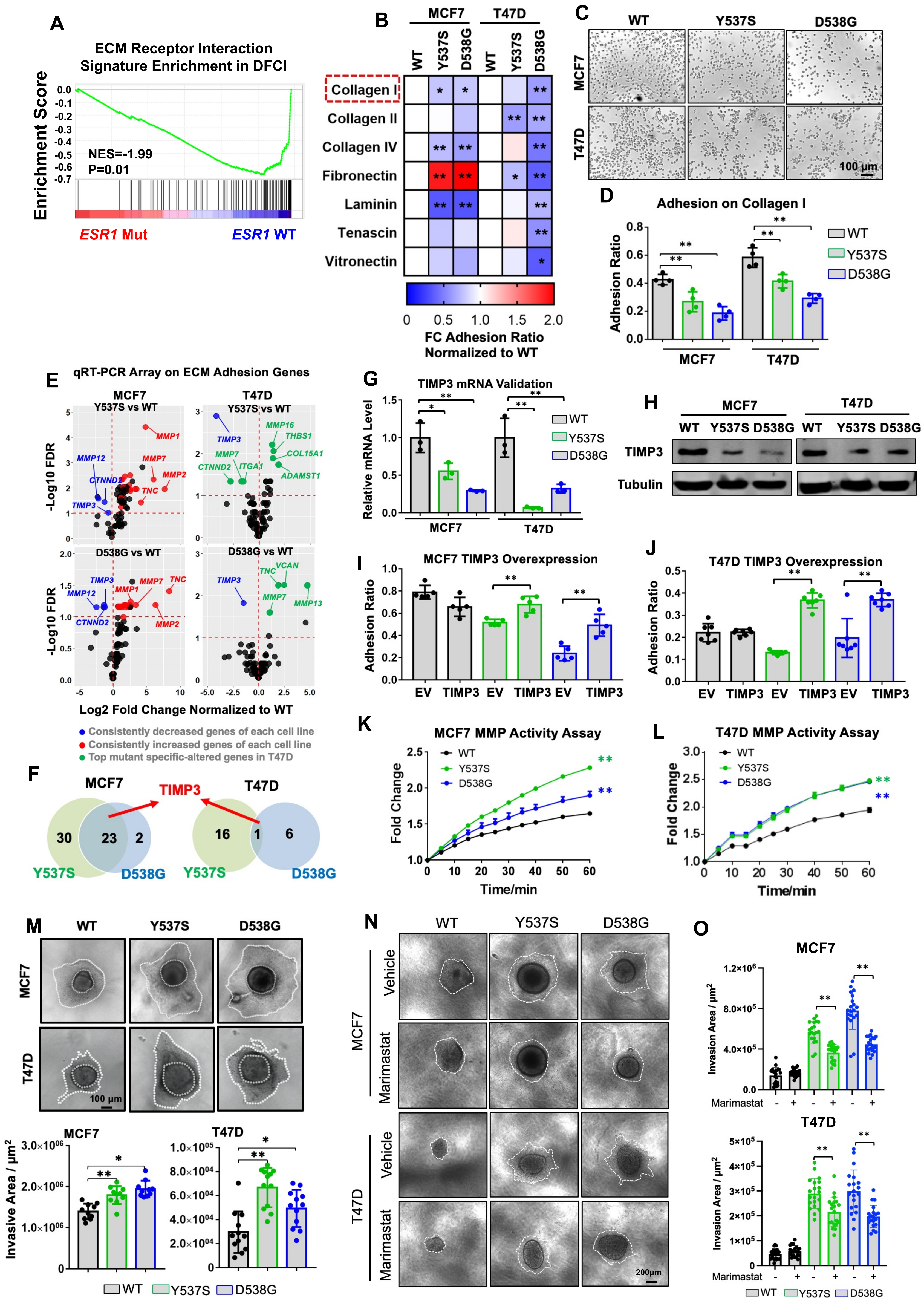
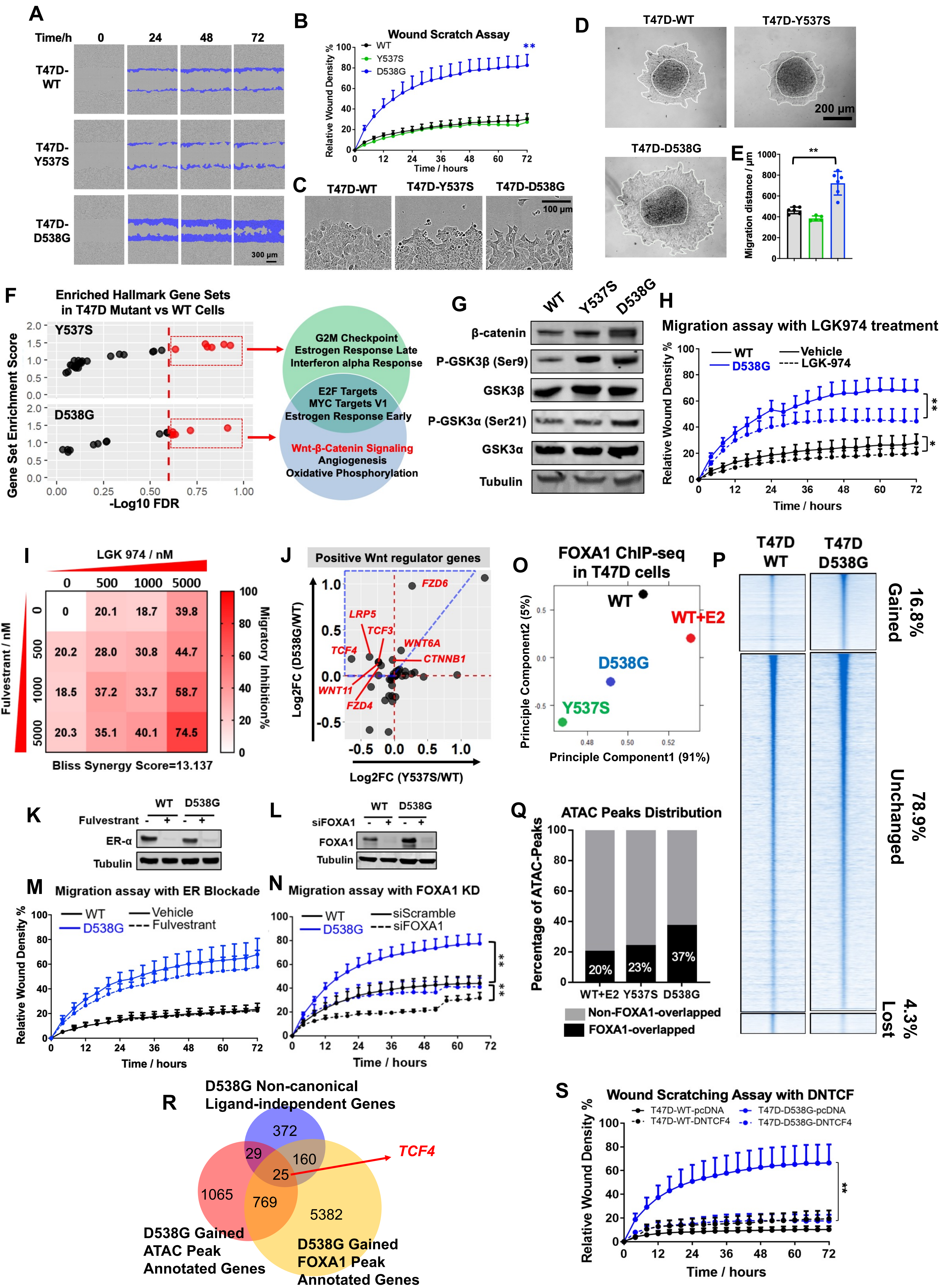


Figure 5



Cancer Research

The Journal of Cancer Research (1916–1930) | The American Journal of Cancer (1931–1940)

Hotspot ESR1 mutations are multimodal and contextual modulators of breast cancer metastasis

Zheqi Li, Yang Wu, Megan E. Yates, et al.

Cancer Res Published OnlineFirst January 25, 2022.

Updated version	Access the most recent version of this article at: doi: 10.1158/0008-5472.CAN-21-2576
Supplementary Material	Access the most recent supplemental material at: http://cancerres.aacrjournals.org/content/suppl/2022/01/22/0008-5472.CAN-21-2576.DC1
Author Manuscript	Author manuscripts have been peer reviewed and accepted for publication but have not yet been edited.

E-mail alerts	Sign up to receive free email-alerts related to this article or journal.
Reprints and Subscriptions	To order reprints of this article or to subscribe to the journal, contact the AACR Publications Department at pubs@aacr.org .
Permissions	To request permission to re-use all or part of this article, use this link http://cancerres.aacrjournals.org/content/early/2022/01/25/0008-5472.CAN-21-2576 . Click on "Request Permissions" which will take you to the Copyright Clearance Center's (CCC) Rightslink site.